

Phase state and viscosity of secondary organic aerosols over China simulated by WRF-Chem

Zhiqiang Zhang^{1,2}, Ying Li^{1,2}, Haiyan Ran^{1,2}, Junling An^{1,2}, Yu Qu^{1,2}, Wei Zhou¹, Weiqi Xu^{1,2}, Weiwei Hu³, Hongbin Xie⁴, Zifa Wang^{1,2}, Yele Sun^{1,2}, Manabu Shiraiwa⁵

¹State Key Laboratory of Atmospheric Boundary Layer Physics and Atmospheric Chemistry, Institute of Atmospheric Physics, Chinese Academy of Sciences, Beijing 100029, China

²College of Earth and Planetary Sciences, University of Chinese Academy of Sciences, Beijing 100049, China

³State Key Laboratory of Organic Geochemistry, Guangzhou Institute of Geochemistry, Chinese Academy of Sciences, Guangzhou 510640, China

⁴Key Laboratory of Industrial Ecology and Environmental Engineering (Ministry of Education), School of Environmental Science and Technology, Dalian University of Technology, Dalian 116024, China

⁵Department of Chemistry, University of California, Irvine, CA 92697-2025, USA

Correspondence to: Ying Li (liying-iap@mail.iap.ac.cn)

Abstract. Secondary organic aerosols (SOA) can exist in liquid, semi-solid or amorphous solid states. Chemical transport models (CTMs), however, usually assume that SOA particles are homogeneous and well-mixed liquids, with rapid establishment of gas-particle equilibrium for simulations of SOA formation and partitioning. Missing the information of SOA phase state and viscosity in CTMs impedes accurate representation of SOA formation and evolution, affecting the predictions of aerosol effects on air quality and climate. We have previously developed a parameterization to estimate the glass transition temperature (T_g) of an organic compound based on volatility and to predict viscosity of SOA. In this study, we apply this method to predict the phase state of SOA particles over China in summer of 2018 using the Weather Research and Forecasting model coupled to Chemistry (WRF-Chem). The simulated T_g of dry SOA ($T_{g,org}$) agrees well with the value estimated from ambient volatility measurements at an urban site in Beijing. For the spatial distributions of $T_{g,org}$, simulations show that at the surface, the values of $T_{g,org}$ range from ~ 287 K to 305 K, with higher values in the northwestern China where SOA particles have larger mass fractions of low volatility compounds. Considering water uptake by SOA particles, the SOA viscosity shows a prominent geospatial gradient that highly viscous or solid SOA particles are mainly predicted in the northwestern China. The lowest and highest SOA viscosity values both occur over the Qinghai-Tibet Plateau that the solid phase state is predicted over dry and high-altitude areas and the liquid phase state is predicted mainly in the south of the plateau with high relative humidity during the summer monsoon season. Sensitivity simulations show that including the formation of extremely low-volatile organic compounds, the percent time that a SOA particle is in the liquid phase state decreases by up to 12 % in the southeastern China during the simulated period. With an assumption that the organic and inorganic compounds are internally mixed in one phase, we show that the water absorbed by inorganic species can significantly lower the simulated viscosity over the southeastern China. This indicates that constraining the uncertainties in

33 simulated SOA volatility distributions and the mixing state of the organic and inorganic compounds would improve
34 prediction of viscosity in multicomponent particles in southeastern China. We also calculate the characteristic mixing
35 timescale of organic molecules in 200 nm SOA particles to evaluate kinetic limitations in SOA partitioning. Calculations
36 show that during the simulated period the percent time of the mixing timescale longer than 1 h is > 70 % at the surface and at
37 500 hPa in most areas of the northern China, indicating that kinetic partitioning considering the bulk diffusion in viscous
38 particles may be required for more accurate prediction of SOA mass concentrations and size distributions over these areas.

39 **1 Introduction**

40 Secondary organic aerosols (SOA) are major components of atmospheric fine particles, impacting air quality, climate and
41 public health (Jimenez et al., 2009; Pöschl and Shiraiwa, 2015). The formation and evolution of SOA involve both chemical
42 reactions and mass transport in the gas and particle phases (Ziemann and Atkinson, 2012). This complexity makes accurate
43 representation of SOA evolution in chemical transport models (CTMs) challenging, leading to a large uncertainty in
44 evaluating SOA impacts on air quality and climate (Kanakidou et al., 2005; Shrivastava et al., 2017).

45 Current CTMs usually assume that SOA particles are homogeneous and well-mixed liquids, with rapid establishment of
46 gas-particle equilibrium applied in simulations of SOA formation and partitioning (Pankow, 1994; Donahue et al., 2006). It
47 has been shown that SOA can exist in liquid (low dynamic viscosity η , $\eta < 10^2$ Pa s), semi-solid (10^2 Pa s $\leq \eta \leq 10^{12}$ Pa s) or
48 solid (amorphous or glassy solid; $\eta > 10^{12}$ Pa s) states, depending on particle chemical composition and atmospheric
49 conditions, such as ambient temperature (T) and relative humidity (RH) (Koop et al., 2011; Reid et al., 2018). Viscosities can
50 be converted to bulk diffusion coefficients via the Stokes-Einstein equation (Einstein, 1905; Seinfeld and Pandis, 2016) or
51 the fractional Stokes-Einstein equation (Price et al., 2016; Evoy et al., 2019; Evoy et al., 2020). The phase state, viscosity,
52 and bulk diffusivity of SOA are important in many aerosol processes. The semi-solid or solid phase state can prolong the
53 equilibration timescales in the gas-particle partitioning, indicating a need of considering kinetic limitations in simulating the
54 SOA partitioning into highly viscous particles (Shiraiwa and Seinfeld, 2012; Roldin et al., 2014; Zaveri et al., 2014; Li and
55 Shiraiwa, 2019). The viscosity of SOA can impact the rates of heterogeneous and multiphase reactions (Marshall et al., 2018;
56 Zhang et al., 2019a), photochemistry (Liu et al., 2018; Dalton and Nizkorodov, 2021; Baboomian et al., 2022), and the
57 uptake of gaseous pollutants (e.g., O₃, OH, N₂O₅, NO₂, NH₃, and SO₂) and water vapor (Abbatt et al., 2012; Kuwata and
58 Martin, 2012; Preston and Zuend, 2022), with implications for accurate predictions of atmospheric chemical composition
59 (Reid et al., 2018). The SOA phase state also affects particle size distribution evolution (Shiraiwa et al., 2013; Zaveri et al.,
60 2022) and ice nucleation pathways (Knopf and Alpert, 2023).

61 Accurate predictions of the viscosity need the information of molecular structures and functional groups (Song et al.,
62 2016; Rothfuss and Petters, 2017; Gervasi et al., 2020; Galeazzo and Shiraiwa, 2022); however, molecular specificity is

63 often unavailable in ambient measurements, leading to the prediction of the phase state of ambient SOA particles difficult.
64 Currently there are only a few methods developed to predict the phase state of ambient SOA particles, and successfully be
65 implemented in CTMs. Li, Shiraiwa and coauthors first developed a parameterization predicting the glass transition
66 temperature (T_g) based on the molar mass (M) and the atomic O/C ratio for carbon-hydrogen (CH) and
67 carbon-hydrogen-oxygen (CHO) compounds with their molar mass less than 450 g mol^{-1} (Shiraiwa et al., 2017). T_g
68 characterizes the temperature at which a phase transition between amorphous solid and semi-solid states occurs (Koop et al.,
69 2011). When the ambient T is higher than T_g , a SOA particle is in a semi-solid or liquid phase state; otherwise, it behaves as
70 an amorphous solid. This parameterization has been successfully coupled into CTMs simulating the SOA phase state over
71 the globe (Shiraiwa et al., 2017) or the U.S. (Schmedding et al., 2020; Li et al., 2021b), showing that semi-solid and
72 amorphous solid phase states frequently occurred over dry lands and in the upper troposphere. Further parameterizations
73 were developed to predict T_g as a function of the saturation mass concentration (C^0) and the O/C ratio of organic compounds,
74 or as a function of C^0 solely, which indirectly included the effect of molecular structure on T_g estimations (Li et al., 2020).
75 This parameterization can be used in the volatility basis set (VBS) framework (Donahue et al., 2006), which is widely
76 adopted in CMTs simulating SOA formation (Lane et al., 2008a; Knote et al., 2015). Rasool et al. (2021) then coupled this
77 new method (Li et al., 2020) into the Weather Research and Forecasting Model coupled to chemistry (WRF-Chem) (Grell et
78 al., 2005; Fast et al., 2006), and the simulations showed that the viscosity of SOA particles could be reasonably predicted
79 during the dry-to-wet transition season in the Amazon rainforest. Li et al. (2020) was also applied in the WRF-Chem
80 simulating the effects of particle phase state on the multiphase chemistry of SOA formation in the Amazon rainforest
81 (Shrivastava et al., 2022; Rasool et al., 2023). Instead of predicting T_g , Maclean et al. (2021) developed parameterizations for
82 viscosity as a function of T and RH based on measured viscosity data of laboratory SOA, and applied the viscosity
83 parameterizations in CTMs to predict the mixing timescales of organic molecules and water molecules within SOA particles
84 on a global scale (Maclean et al., 2017; Maclean et al., 2021). It is needed to conduct more simulations to investigate the
85 SOA phase state varied with locations and the time. Simulations of the SOA phase state in China on a regional scale have not
86 been available.

87 Investigations in the particle phase state over China are currently focused on field observations and laboratory
88 experiments. Bounce factor measurements showed that submicrometer particles can be semi-solid in clear days and liquid in
89 hazy days in Beijing, China (Liu et al., 2017). The phase state of $\text{PM}_{2.5}$ (particulate matter with an aerodynamic diameter \leq
90 $2.5 \mu\text{m}$) was found to be mostly semisolid to solid in winter Beijing based on the measurements using optical microscopy
91 combined with the poke-and-flow technique (Song et al., 2022). The RH-dependent viscosity of the proxies of actual
92 ambient particles in Beijing was also investigated based on dual optical tweezers (Tong et al., 2022). The phase state of
93 submicrometer particles in Beijing was retrieved from a polarization lidar that has the potential to infer the vertical profiles
94 of phase state (Tan et al., 2020). The phase state of traffic-related secondary aerosols in Beijing may have a distinguished

95 diurnal variation (Meng et al., 2021). The biomass burning aerosols, collected near a farmland in Yangtze River Delta, China,
96 were found to exist in the non-solid phase state at relatively dry conditions (Liu et al., 2021).

97 These measurements indicate that the particle phase state over China is highly variable under different atmospheric
98 conditions. It is important to know the spatial distributions and time variations of the SOA phase state and viscosity in
99 multicomponent particles to better quantify the aerosol effects on air quality, which, however, has not been investigated over
100 China with air quality models on a regional scale. Here we use the WRF-Chem model simulated SOA volatility distributions
101 to estimate the glass transition temperature and viscosity of SOA particles over China based on the parameterizations
102 developed in Li et al. (2020). We further calculate the diffusion coefficients and mixing timescales of organic molecules
103 within SOA, which has implications in how to properly treat the SOA partitioning (instantaneous equilibrium vs. kinetic
104 partitioning) in CTMs. As volatility and viscosity are closely related, we conduct a sensitivity calculation to evaluate the
105 effects of the simulated SOA volatility distributions on viscosity estimations. We also conduct a sensitivity calculation to
106 investigate how the water absorbed by inorganic components in $PM_{2.5}$ affects viscosity estimations, which has implications
107 in predicting the viscosity of internally mixed ambient particles.

108 **2 Methods**

109 **2.1 WRF-Chem model configuration**

110 We use the WRF-Chem model version 3.7.1 (Grell et al., 2005; Fast et al., 2006) and simulate the period from 20 May to 23
111 June 2018 with a spin-up period of 7 days (May 13 – 19). We set up two domains (Fig. S1 in the Supplement) with the
112 horizontal resolutions of 81 km and 27 km, respectively, and 18 vertical layers are applied from the surface up to 100 hPa.
113 The meteorological initial and boundary conditions are from the National Centers for Environmental Prediction (NCEP)
114 Global Forecast System (GFS) final (FNL) reanalysis data. The outputs of a global chemical transport model MOZART-4
115 (Emmons et al., 2010) provide initial and boundary conditions of chemical species over the outer domain (Fig. S1 in the
116 Supplement). Anthropogenic emissions are from the MIX 2010 inventory for Asia (Li et al., 2017) and the MEIC 2016
117 inventory for China (<http://meicmodel.org.cn>) (Zheng et al., 2018). Biogenic emissions are calculated from the Model of
118 Emissions of Gases and Aerosols from Nature (MEGAN2.1) (Guenther et al., 2012).

119 The utilized physical and chemical schemes are given in Table S1. We use the MOZART-4 mechanism (Emmons et al.,
120 2010) for the gas-phase chemistry. The MOSAIC (Model for Simulating Aerosol Interactions and Chemistry) aerosol module
121 (Zaveri et al., 2008) is applied for the aerosol chemistry and we represent aerosol particles with 4-size sections having dry
122 diameters ranging from 0.039 μm to 10 μm (Knote et al., 2015). SOA formation is treated with the 1-D volatility basis set
123 (VBS) approach (Donahue et al., 2006) which has been implemented into the MOSAIC aerosol module (Lane et al., 2008a;
124 Ahmadov et al., 2012). Five volatility bins are considered (effective saturation mass concentrations C^* of 10^{-4} , 1, 10, 100,

125 and $1000 \mu\text{g m}^{-3}$ at 298 K) in the official version 3.7.1 of the WRF-Chem model, with the enthalpy of vaporization (ΔH_{vap})
 126 values of 40, 131, 120, 109, and 98 kJ mol^{-1} used in each volatility bin (Knote et al., 2015). We follow Knote et al. (2015)
 127 with SOA mass yields adopted for four volatility bins (1, 10, 100, and $1000 \mu\text{g m}^{-3}$). Further gas-phase aging is simulated
 128 through OH oxidation of SOA vapors with a fixed rate of $1.0 \times 10^{-11} \text{ cm}^3 \text{ molec}^{-1} \text{ s}^{-1}$, with products shifted down one
 129 volatility bin (Murphy and Pandis, 2009), e.g., the condensable vapors with C^* of $1 \mu\text{g m}^{-3}$ react with OH forming surrogate
 130 species in the lowest volatility bin (C^* of $10^{-4} \mu\text{g m}^{-3}$). The partitioning of organic compounds between the gas and particle
 131 phases is simulated based on Pankow (1994) which is implemented in MOSAIC (Shrivastava et al., 2011). We apply glass
 132 transition temperature and viscosity calculations to WRF-Chem model output for traditional SOA formed from the oxidation
 133 of volatile organic compounds including alkanes, alkenes, aromatics, isoprene, and monoterpenes (Lane et al., 2008b).

134 2.2 Glass transition temperature and viscosity calculations

135 The glass-transition temperature of SOA products in each volatility bin at dry conditions ($T_{g,i}$) is calculated as a function of
 136 the saturation mass concentration at 298 K (C^0) using the parameterization (Eq. 1) developed in our previous study (Li et al.,
 137 2020). We assume ideal thermodynamic mixing that C^0 is equal to C^* , which is often applied in the VBS (Donahue et al.,
 138 2011).

$$T_{g,i} = 288.70 - 15.33 \times \log_{10}(C^0) - 0.33 \times [\log_{10}(C^0)]^2 \quad (1)$$

139 The T_g of mixtures of dry SOA compounds ($T_{g,\text{org}}$) is calculated by the Gordon–Taylor equation (Gordon and Taylor,
 140 1952), with the Gordon–Taylor constant (k_{GT}) assumed to be 1 (Dette et al., 2014):

$$T_{g,\text{org}} = \sum_i \omega_i T_{g,i} \quad (2)$$

141 where ω_i is the mass fraction of SOA products in each volatility bin simulated by the VBS module in WRF-Chem.

142 The particle phase state depends strongly on water content in particles, as water can act as a plasticizer to decrease
 143 viscosity (Mikhailov et al., 2009; Koop et al., 2011). The mass concentration of water absorbed by SOA particles under
 144 humid conditions is estimated using the effective hygroscopicity parameter (κ) (Petters and Kreidenweis, 2007) as:

$$m_{\text{H}_2\text{O}} = \left(\frac{a_w}{1 - a_w} \right) \frac{\kappa \rho_w m_{\text{SOA}}}{\rho_{\text{SOA}}} \quad (3)$$

145 where a_w is water activity calculated as $a_w = \text{RH}/100$ and ρ_w is the density of water. m_{SOA} is the simulated total mass
 146 concentrations of traditional SOA. The density of SOA particles (ρ_{SOA}) is assumed to be 1.5 g cm^{-3} (Knote et al., 2015). κ
 147 assumed to be 0.1 based on previous studies (Gunthe et al., 2009; Duplissy et al., 2011; Wu et al., 2013) and consistent with
 148 the value used in our previous global SOA phase state simulations (Shiraiwa et al., 2017).

149 T_g of organic-water mixtures is also calculated by the Gordon–Taylor equation (Eq. 4) with k_{GT} suggested to be 2.5
 150 (Koop et al., 2011).

$$T_g(\omega_{\text{org}}) = \frac{(1 - \omega_{\text{org}})T_{g,w} + \frac{1}{k_{\text{GT}}} \omega_{\text{org}} T_{g,\text{org}}}{(1 - \omega_{\text{org}}) + \frac{1}{k_{\text{GT}}} \omega_{\text{org}}} \quad (4)$$

151 where ω_{org} is the mass fraction of the simulated SOA species in organic-water mixtures. The glass transition temperature of
 152 pure water ($T_{g,w}$) is 136 K (Kohl et al., 2005). Based on $T_g(\omega_{\text{org}})$, viscosity can be calculated with the
 153 Vogel–Tammann–Fulcher (VTF) equation (Angell, 1991): $\eta = \eta_{\infty} e^{\frac{T_0 D}{T - T_0}}$, where η_{∞} is the viscosity at infinite temperature
 154 (10^{-5} Pa s, Angell (1991)). D is the fragility parameter which is adopted to be 10 based on our previous study in DeRieux
 155 and Li et al. (2018). T_0 is the Vogel temperature calculated as $T_0 = \frac{39.17 T_g(\omega_{\text{org}})}{D + 39.17}$. We further calculate the bulk diffusion
 156 coefficient (D_b) of organic molecules with a radius of 0.4 nm (Maclean et al., 2021) and water molecules in SOA particles
 157 based on predicted viscosity and the fractional Stokes–Einstein equation (Price et al., 2016; Evoy et al., 2019; Evoy et al.,
 158 2020), which is detailed in the Supplement. The mixing timescales of molecules (τ_{mix}) within SOA particles is calculated as
 159 $\tau_{\text{mix}} = d_p^2 / (4\pi^2 D_b)$ (Seinfeld and Pandis, 2016), where d_p is the particle diameter. The d_p is assumed to be 200 nm
 160 (Maclean et al., 2021) when we calculate τ_{mix} .

161 2.3 Sensitivity simulations

162 Table 1 lists all the performed simulations. In the base case, we update the C^* in the lowest volatility bin from $10^{-4} \mu\text{g m}^{-3}$ in
 163 the official WRF-Chem v3.7.1 to $0.1 \mu\text{g m}^{-3}$ based on the ambient volatility observations (referring to Section 2.4 and Fig. 1),
 164 and calculate the ΔH_{vap} in the lowest volatility bin using the semi-empirical parameterization in Epstein et al. (2010), leading
 165 to a value of 142 kJ mol^{-1} . To evaluate the effects of simulated SOA volatility distributions on phase state estimations, we
 166 conduct a simulation (sensitivity case A) following the default setting in the model assuming that the lowest C^* is $10^{-4} \mu\text{g m}^{-3}$
 167 at 298 K, with ΔH_{vap} of 40 kJ mol^{-1} (Knote et al., 2015). A smaller ΔH_{vap} indicates less dependence of volatility on
 168 temperature variations. In the sensitivity case B, we increase the simulated RH by a factor of 10 % as we find that the
 169 simulated RH values are smaller than the observations (Section 3.1). In the base case and sensitivity cases A and B, we
 170 predict T_g for SOA-water mixtures accounting for the SOA-influenced water uptake solely, assuming that SOA particles are
 171 externally mixed with inorganic compounds such as sulfate and nitrate. In the sensitivity case C, we assume that the organic
 172 and inorganic compounds are internally mixed in one phase and include the water absorbed by inorganic compounds in
 173 viscosity calculations. The water associated with inorganics is calculated by the MOSAIC module coupled in WRF-Chem.

174 2.4 Observation

175 The observation data measured at an urban site in the Institute of Atmospheric Physics (IAP), Chinese Academy of Sciences
 176 ($39^{\circ}58'28''$ N, $116^{\circ}22'16''$ E) in Beijing (Fig. S1 in the Supplement) are used to compare with the simulation results of the
 177 WRF-Chem model. The aerosol volatility was measured from 20 May to 23 June in 2018, using a thermodenuder coupled

178 with an Aerodyne high-resolution aerosol mass spectrometer (Xu et al., 2019). The volatility distributions of oxygenated
179 organic aerosols (OOA) resolved from positive matrix factorization (PMF) were estimated using a dynamic mass transfer
180 model (Riipinen et al., 2010). The volatility of OOA was found to be distributed in six logarithmically spaced C^* bins
181 including 0.001, 0.01, 0.1, 1, 10, and 100 $\mu\text{g m}^{-3}$, based on the best fits between the measured and predicted thermograms
182 using the methods in Karnezi et al. (2014). Chemical species including organics (Org), sulfate (SO_4^{2-}), nitrate (NO_3^-), and
183 ammonium (NH_4^+) in $\text{PM}_{2.5}$ were measured using an Aerodyne time-of-flight aerosol chemical speciation monitor (Fröhlich
184 et al., 2013) equipped with a capture vaporizer and $\text{PM}_{2.5}$ lens, with the details described in Li et al. (2023). The OOA factor
185 was identified with the PMF analysis. We obtain the mass concentrations of $\text{PM}_{2.5}$ from the Olympic Center observation site
186 (<http://zx.bjmemc.com.cn>) which is ~ 4 km from the IAP site (Fig. S1 in the Supplement). Meteorological parameters
187 including RH and T are from the Beijing meteorological tower at the IAP site.

188 3 Results

189 3.1 Simulations in Beijing and the comparison with observations

190 The comprehensive model evaluations were conducted in our previous studies, showing that the WRF-Chem model
191 reasonably captured the magnitudes and spatial distributions of concentrations of major air pollutants over China (Li et al.,
192 2011; Li et al., 2014; Li et al., 2015; Qu et al., 2019; Zhang et al., 2022). Here we focus on the comparison of simulations
193 and observations at the IAP site during 20 May – 23 June 2018 when the observed volatility distributions are available (Xu et
194 al., 2019).

195 Figure 1 shows the average volatility distributions of observed OOA and simulated SOA at the IAP site. The C^* of OOA
196 spans from 0.001 $\mu\text{g m}^{-3}$ to 100 $\mu\text{g m}^{-3}$, with an average value of 1.16 $\mu\text{g m}^{-3}$. The semi-volatile organic compounds (SVOC;
197 $0.3 < C^0 < 300 \mu\text{g m}^{-3}$) and the low-volatile organic compounds (LVOC; $3 \times 10^{-4} < C^0 < 0.3 \mu\text{g m}^{-3}$) (Donahue et al., 2012)
198 contribute 66.3 % and 33.7 % to OOA concentrations, respectively (Xu et al., 2019). The $T_{\text{g,org}}$ estimated from the observed
199 OOA volatility distributions is 286.7 K. Figure 1a shows the simulated volatility distributions of SOA with five C^* bins set to
200 be 0.1, 1, 10, 100, and 1000 $\mu\text{g m}^{-3}$ at 298 K, and ΔH_{vap} of 142, 131, 120, 109, and 98 kJ mol^{-1} used in the five C^* bins,
201 respectively (base case in Table 1). In this base case simulation, the SOA consists of 64.5 % SVOC and 35.3 % LVOC, and
202 most of the SVOC species are located in the C^* bin of 1 $\mu\text{g m}^{-3}$. The simulated SOA in Fig. 1a has an average C^* of 0.64 μg
203 m^{-3} and $T_{\text{g,org}}$ of 291.5 K, close to the values estimated from the volatility distributions of OOA. Figure 1b shows the
204 simulated volatility distributions of SOA with the lowest C^* bin set to be 0.0001 $\mu\text{g m}^{-3}$ at 298 K with ΔH_{vap} of 40 kJ mol^{-1} ,
205 following the default option in the official WRF-Chem model 3.7.1 (Knote et al., 2015). In this sensitivity simulation (case A
206 in Table 1), the SOA consists of 40.4 % extremely low-volatile organic compounds (ELVOC; $C^0 < 3 \times 10^{-4} \mu\text{g m}^{-3}$), which are
207 not determined in the observed OOA, leading to a much lower average C^* (0.03 $\mu\text{g m}^{-3}$) and a higher $T_{\text{g,org}}$ (309.0 K)

208 compared to the observations. In the following we estimate the $T_{g,org}$ and viscosity of SOA using the simulated volatility
209 distributions in the base case with the lowest C^* bin set as $0.1 \mu\text{g m}^{-3}$ at 298 K. The impacts of volatility distributions with
210 the incorporation of ELVOC (Fig. 1b) on viscosity estimations are evaluated in section 3.3.

211 Figure 2 shows that the model relatively well reproduces the observed hourly variations of RH, T , mass concentrations
212 of $\text{PM}_{2.5}$ and its major inorganic components (Figs. 2a – f), with the index of agreement (IOA, defined in the Supplement)
213 varied from ~ 0.70 for inorganic components to a higher value of 0.93 for T (Table S2 in the Supplement). The simulated
214 values of RH are constantly lower than the observations, with the mean bias (MB) being -10.97% (Table S2 in the
215 Supplement). The underestimation of RH observations was also found at other meteorological sites in the North China Plain
216 in our previous studies (Qu et al., 2019; Zhang et al., 2022), which would affect the SOA viscosity estimations. The effects
217 of RH on the viscosity estimations are evaluated in section 3.3. Figure 2g shows that the model could generally reproduce
218 the observed temporal variations of OOA concentrations, but largely underestimates the observation peaks ($\text{MB} = -5.88 \mu\text{g}$
219 m^{-3} , the normalized mean bias $\text{NMB} = -53.28\%$, Table S2 in the Supplement). Incorporation of the SOA formed from
220 intermediate-volatile organic compounds (IVOCs) (Miao et al., 2021; Chang et al., 2022) would increase the simulated SOA
221 concentrations, which is beyond the scope of this study and will be considered in our future work. The simulated SOA mean
222 concentration is $5.15 \mu\text{g m}^{-3}$. Although it is lower than the observed value of $11.03 \mu\text{g m}^{-3}$, this difference in the simulated
223 and observed SOA concentrations would not affect the viscosity predictions significantly. The SOA viscosity has a much
224 closer relation with the volatility rather than its mass loadings (Champion et al., 2019; Li et al., 2020). In our previous study
225 we estimated $T_{g,org}$ and viscosities at different OA mass loadings varied from 1 to $1000 \mu\text{g m}^{-3}$, showing that the simulated
226 viscosities were very similar, particularly when RH was higher than 50% (DeRieux et al., 2018).

227 As the WRF-Chem model underestimates the observed RH at the IAP site, we calculate the SOA viscosity using the
228 simulated and observed RH, respectively. Figure 2h shows that the viscosities calculated at the two conditions are similar at
229 most times during the simulated period, ranging mainly from $\sim 10^2 \text{ Pa s}$ to 10^{10} Pa s , with a median value of $\sim 10^7 \text{ Pa s}$,
230 indicating that a semi-solid phase state frequently occurs. The underestimations of the observed RH by WRF-Chem mainly
231 impact the phase state estimations at relatively high RH. For example, SOA particles occur as liquid when the observed RH
232 is higher than $\sim 75\%$; however, they remain in a semi-solid phase state at the simulated RH. The bulk diffusion coefficients
233 (D_b) of organic molecules range from 10^{-18} to $10^{-11} \text{ cm}^2 \text{ s}^{-1}$ at the simulated RH (Fig. 2i), leading to the mixing timescales
234 within 200 nm SOA particles being seconds to years, with 61% of the time > 1 hour (Fig. S2 in the Supplement). We
235 highlight the mixing timescale of 1 hour as the time step adopted in CTMs is often $\sim 0.5 - 1$ hour (Maclean et al., 2021).
236 Current CTMs usually assume that the gas-particle partitioning of SVOCs reaches equilibrium quickly within the time step
237 (Pankow, 1994; Donahue et al., 2006). When the mixing timescales of organics within SOA particles are $\leq \sim 1$ hour, the
238 instantaneous equilibrium is a reasonable assumption. However, when the mixing timescales of organics are longer than ~ 1
239 hour, non-equilibrium between the gas phase and the particle phase, i.e., the kinetic partitioning may need to be considered in

240 simulating the SOA formation in CTMs (Shiraiwa and Seinfeld, 2012; Zaveri et al., 2018; Li and Shiraiwa, 2019; Zaveri et
241 al., 2020; He et al., 2021; Jathar et al., 2021; Maclean et al., 2021; Shiraiwa and Pöschl, 2021; Shrivastava et al., 2022).

242 The vertical profiles of SOA viscosity exhibit diurnal variations. Figure 3a shows the median diurnal and vertical
243 profiles of predicted SOA viscosity at the IAP site. The SOA particles remain highly viscous ($\sim 10^7 - 10^8$ Pa s) at the surface,
244 with a higher viscosity occurring from late afternoon to early evening, during which the RH is less than 20 %, lower than the
245 rest time of the day (Fig. S3 in the Supplement). The SOA particles become more viscous at higher altitudes than the surface
246 and adopt the phase transition from a semi-solid phase to a solid phase at ~ 4 km at the IAP site. The predicted altitude with
247 the phase transition is ~ 2 km higher than our previous global model prediction for the region of East China which was an
248 average of five years' simulations (Shiraiwa et al., 2017). Tan et al. (2020) inferred the phase state of submicrometer
249 particles in Beijing from the surface to an altitude of ~ 1 km using a polarization lidar and found that the particle phase state
250 exhibits a vertical variation. Further observations of SOA viscosity at high altitudes are needed to better understand the
251 viscosity vertical profiles and validate our predictions. Figure 3b shows that the mixing timescales for organic molecules
252 within 200 nm SOA particles are approximately 1 hour at the surface, and longer than ~ 10 hours at altitudes higher than 1
253 km, indicating that kinetic limitations in the gas-particle partitioning may be required to accurately predict SOA mass
254 concentrations in summer Beijing, particularly in the upper planetary boundary layer and the free troposphere.

255 3.2 Simulated glass transition temperature and viscosity of SOA particles over China

256 The glass transition temperature of the dry organic phase ($T_{g,org}$) shows a geospatial gradient over China. Figure 4a shows the
257 median surface values of $T_{g,org}$ calculated in the base simulation (Table 1). $T_{g,org}$ ranges from $\sim 287 - 305$ K over most areas of
258 China, with lower values occurring mainly over the southeast and higher values over the northwest. The $T_{g,org}$ range
259 simulated by the WRF-Chem model is consistent with our previous global simulations of $T_{g,org}$ that varied from ~ 285 K to
260 310 K at the surface over China (Shiraiwa et al., 2017). The geospatial variation in $T_{g,org}$ is related to the simulated SOA
261 volatility distributions. Figure 4b shows the mass fractions of SOA species distributed in the lowest volatility bin (SOAX
262 with $C^* = 0.1 \mu\text{g m}^{-3}$ at 298 K). The mass fractions of SOAX are mostly 20 – 35 % in the southeastern China, indicating that
263 the majority of the simulated SOA formed from VOCs is semi-volatile. In these areas, the simulated SOA mass
264 concentrations are higher than the other locations of China (Fig. S4 in the Supplement) (Li et al., 2022), which is favorable
265 for more SVOCs partitioning into the particle phase, leading to relatively low values of $T_{g,org}$ (Fig. 4a). LVOCs are more
266 frequently contained in aged SOA particles in remote areas, e.g., some areas in the northwestern China where the SOA mass
267 concentrations are very low, resulted in higher $T_{g,org}$ values.

268 The relative humidity plays an important role in regulating SOA viscosity (Koop et al., 2011). Considering the water
269 uptake by SOA particles in the phase state estimations, the predicted geospatial patterns in the viscosity (Fig. 5a) and RH
270 (Fig. S4 in the Supplement) are very similar with each other, particularly in southern and northeastern China. SOA particles

271 are predicted to mainly be liquid or with a low viscosity ($< 10^4$ Pa s) in the southeast. Figure 5b shows the frequency of
272 liquid phase state, which is calculated as the percent time that an organic aerosol particle is in the liquid phase state during
273 the simulated period. The frequency of liquid particles varies from $\sim 30\%$ to 70% in the southeastern China. The lowest
274 viscosity with the highest frequency of liquid particles occurs over the southern Tibetan Plateau where RH is very high (Fig.
275 S4), which is contributed by summer monsoons and regional moisture recycling (Dong et al., 2016). The SOA particles in
276 the central and northeastern China are predicted to be semi-solid, with the viscosity varied from 10^5 to 10^8 Pa s (Fig. 5a).
277 Highly viscous ($\eta > 10^8$ Pa s) or solid SOA particles are mainly found in the northwest, particularly over the northern Tibetan
278 Plateau where the ambient temperatures are lower than other areas of China (Fig. S4). The frequency of liquid SOA particles
279 in most areas with the latitude higher than 30°N is less than 20% (Fig. 5b).

280 The simulated geospatial pattern in SOA viscosity over China agrees with previous global simulations and ambient
281 measurements. Our previous global simulations predicted a lower viscosity ($\eta < 10^3$ Pa s) in SOA particles in southeastern
282 China and a higher viscosity ($\eta > 10^8$ Pa s) in northwestern China (Shiraiwa et al., 2017; Li et al., 2020), similar to the
283 WRF-Chem simulations in this study. Interestingly, the occurrence of liquid particles over the southern Tibetan Plateau in
284 summer simulated by the WRF-Chem was not found in our previous global predictions, which was an average of five years'
285 simulations (Shiraiwa et al., 2017). The semi-solid phase state of SOA particles simulated in Beijing is consistent with both
286 particle bounce measurements (Liu et al., 2017) and the $\text{PM}_{2.5}$ phase state determined by the poke-and-flow technique (Song
287 et al., 2022). The simulated viscosity of SOA particles is 0.15 Pa s in Shenzhen, a coastal urban city in southeastern China,
288 which also agrees with the findings in the previous bounce measurements indicating that the submicron particles in
289 Shenzhen are in the liquid state (Liu et al., 2019).

290 The phase state of SOA particles is affected by ambient conditions and the particle chemical composition (Koop et al.,
291 2011). Figure 6 shows the median values of viscosity as a function of RH, T and the mass fraction of low-volatility
292 compound (SOAX with C^* of $0.1 \mu\text{g m}^{-3}$ at 298 K) calculated for selected regions in the northern China, southern China,
293 northern Qinghai-Tibet Plateau, and southern Qinghai-Tibet Plateau as specified by white boxes in Fig. 5a. There is a strong
294 inverse relationship between SOA viscosity and relative humidity with high RH ($> \sim 60\%$) as the dominant factor
295 determining the phase state of SOA particles. When RH is lower than $\sim 60\%$, the predicted viscosity is affected by both RH
296 and T . For example, the SOA particles occur mainly as solid over the Northern Qinghai-Tibet Plateau while occur as
297 semi-solid over the Northern China within similar RH ranges ($20\% < \text{RH} < 60\%$); the reason is that the ambient T over the
298 Northern Qinghai-Tibet Plateau is much lower ($\sim 20\text{ K}$ lower) than the Northern China (Fig. 6b). When RH is relatively low,
299 the viscosity of SOA particles is also influenced by particle chemical composition, i.e., the SOA particles composed of high
300 mass fractions of low volatility compounds tend to have higher viscosity values (Fig. 6c). RH is the main factor driving the
301 diurnal variations of SOA viscosity in our simulations. Figure S5 in the Supplement shows that SOA particles have higher
302 viscosity in the daytime than the nighttime as RH in the daytime is lower than the nighttime (Fig. S6). Compared to the

303 northern China, the southern China exhibits stronger diurnal variations in SOA viscosity that SOA particles occur mainly as
304 semi-solid in the daytime and liquid in the nighttime. Highly viscous or solid SOA particles are found in the northern China
305 during both daytime and nighttime (Fig. S5).

306 The bulk diffusion coefficient is an important parameter determining the mass-transport and mixing rates, which can be
307 predicted by the particle viscosity through the fractional Stokes-Einstein relation (see the Method section and the
308 Supplement). The D_b of organic molecules is predicted to be $> \sim 10^{-10} \text{ cm}^2 \text{ s}^{-1}$ in the southern China. The highest value is
309 $\sim 10^{-5} \text{ cm}^2 \text{ s}^{-1}$ occurring in liquid SOA particles in the southern Tibetan Plateau (Fig. 7a) because of the very low viscosity
310 simulated over this region (Fig. 5a). The D_b of organic molecules within semisolid SOA particles is $\sim 10^{-18} - 10^{-10} \text{ cm}^2 \text{ s}^{-1}$ in
311 the central and northeastern China, and lower than $\sim 10^{-18} \text{ cm}^2 \text{ s}^{-1}$ in highly viscous and solid particles in most areas of the
312 northwestern China. Figure 7b shows the percent time that the mixing timescale of organic molecules in 200 nm particles is
313 less than 1 h in the entire simulation period. The mixing timescale is found nearly always less than 1 h in the southeastern
314 region of the “Hu Huanyong Line”. The “Hu Huanyong Line”, proposed by the Chinese geographer Huanyong Hu, divides
315 China into two parts based on contrasting population densities (Hu, 1935), which was found also useful characterizing the
316 drought conditions, with the northwestern region much dryer than the southeastern region (Zeng et al., 2021). The mixing
317 timescale of organic molecules in highly viscous or solid SOA particles in the northwest of the “Hu Huanyong Line” is often
318 longer than 1 h (the frequency $> 70 \%$), indicating that in these areas kinetic limitations of bulk diffusion should be
319 considered in SOA partitioning. Compared to the diffusion coefficients of organic molecules, the D_b of water molecules in
320 SOA particles at the surface is several orders of magnitude larger, with the values higher than $10^{-10} \text{ cm}^2 \text{ s}^{-1}$ in the southeast,
321 and as low as $\sim 10^{-13} \text{ cm}^2 \text{ s}^{-1}$ in the northwestern China (Fig. 7c). The mixing timescales of water molecules in SOA particles
322 with a diameter of 200 nm are of the order of milliseconds in the southeast and seconds in the northwest of China (Fig. S7 in
323 the Supplement), indicating that the activation of cloud condensation nuclei would not be inhibited, in agreement with our
324 previous global simulations (Shiraiwa et al., 2017).

325 Figure 8 shows the simulated $T_{g,\text{org}}$ and the phase state of SOA particles, as well as the mixing timescale of organic
326 molecules in SOA particles at 500 hPa. The $T_{g,\text{org}}$ ranges from $\sim 285 \text{ K} - 295 \text{ K}$, lower than the $T_{g,\text{org}}$ simulated at the surface
327 (Fig. 8a). The reason is that the mass fractions of LVOCs (SOAX with C^* of $0.1 \mu\text{g m}^{-3}$ at 298 K) at 500 hPa (Fig. S8 in the
328 Supplement) are smaller than the surface values (Fig. 4b). The low temperature at 500 hPa is favorable for SVOCs
329 partitioned into the particle phase, thus compared to the surface conditions, there is less semi-volatile vapors undergoing the
330 further gas-phase aging forming SOAX species. The percent time that an organic aerosol particle is in the liquid phase state
331 (the frequency of liquid SOA particles) at 500 hPa in the southeastern China is 20 – 35 % (Fig. 8b), which is $\sim 20 \%$ lower
332 than the surface values (Fig. 5b). In the northern China, the frequency of liquid SOA particles at 500 hPa is similar to the
333 results at the surface, which is related to the RH spatial patterns (Fig. S9 in the Supplement). The mixing timescale of
334 organic molecules in 200 nm SOA particles is frequently longer than 1 h at 500 hPa, with the frequency $> 70 \%$ in the

335 northern China and ~ 40 % in the southeastern China (Fig. 8c). The τ_{mix} is relatively short (the frequency of $\tau_{\text{mix}} \leq 1$ h being ~
336 80 %) in some areas of the southwestern China at 500 hPa, where relatively high RH could occur (Fig. S9 in the Supplement)
337 in the season of summer monsoon (Huang et al., 1998).

338 **3.3 Sensitivity simulations**

339 **3.3.1 Impacts of volatility distributions on phase state estimations**

340 The volatility and viscosity of organic aerosols are closely related (Rothfuss and Petters, 2017; Shiraiwa et al., 2017;
341 Champion et al., 2019; Zhang et al., 2019b; Li et al., 2020). In this section we conduct sensitivity simulations (case A, Table
342 1) to evaluate how the simulated volatility distributions affect the phase state estimations. The lowest C^* bin in the base case
343 is $0.1 \mu\text{g m}^{-3}$ at 298 K, with ΔH_{vap} of 142 kJ mol^{-1} , which does not incorporate ELVOC species at the room temperature. The
344 sensitivity simulation (case A) adopts the default setting in the official WRF-Chem model v3.7.1, assuming that the lowest
345 C^* is $0.0001 \mu\text{g m}^{-3}$ at 298 K, with ΔH_{vap} of 40 kJ mol^{-1} (Knote et al., 2015). Figure 9a shows that including these ELVOCs at
346 298 K with a relatively small ΔH_{vap} mainly affect the $T_{\text{g,org}}$ simulated over remote areas, e.g., the northwestern China and the
347 marine areas, where the simulated $T_{\text{g,org}}$ is increased by 30 – 40 K. In other regions of China, the changes in $T_{\text{g,org}}$ are less
348 than 25 K. Although consideration of these ELVOCs could affect the simulated $T_{\text{g,org}}$ at the surface obviously in remote areas,
349 i.e., the northwestern China, it does not impact the predicted frequency of the occurrence of a liquid phase state (Fig. 9b), as
350 in these dry areas the SOA particles are highly viscous. Including ELVOC formation at 298 K (ΔH_{vap} of 40 kJ mol^{-1}) mainly
351 affects the phase state estimations in areas with a moderate humidity. For example, in some areas of the southeastern China
352 with ~ 70 % RH, the SOA particles are predicted to be more viscous, with the frequency of a liquid phase state decreasing by
353 up to 12 % (Fig. 9b). These results indicate that the SOA phase state estimations in the base and sensitivity case A are
354 generally in agreement in the simulated episode in this study. Ambient measurements of organic aerosol volatility
355 distributions are still sparse over China. A recent field study showed that the ELVOCs contributed more than half to the OA
356 mass observed at a regional background site near the Bohai Sea (Feng et al., 2023), which resulted in an estimated viscosity
357 much higher than our WRF-Chem simulations. More field volatility distribution measurements should be conducted over
358 China to further evaluate the effects of ELVOCs and how to choose reasonable values of the enthalpy of vaporization that
359 would affect phase state estimations.

360 **3.3.2 Impacts of RH and the water absorbed by inorganics on phase state estimations**

361 RH is an important parameter affecting the phase state estimations. We perform a sensitivity calculation (case B, Table 1)
362 with the simulated RH increased by a factor of 10 % to compensate for the fact that the current model underestimates the
363 observed RH as shown in Fig. 2 and found in our previous simulations (Qu et al., 2019; Zhang et al., 2022). The increases in
364 simulated RH lead to more occurrence (the liquid frequency increased by 10 – 20 %) of liquid SOA particles in southeastern

365 China where the predicted RH is ranged mainly from 70 to 80 % (Fig. S4 in the Supplement), with very limited effects in
366 phase state predictions in relatively dry areas, e.g., the northern China (Fig. 10a).

367 Besides RH, the mixing state of the organic and inorganic species in atmospheric particles also plays an important role
368 in the phase state of ambient particles. The SOA components are assumed to be phase separated from inorganic compounds
369 in particles in our base simulation, which is consistent to recent ambient observations showing that the phase separation with
370 an organic-rich shell and an inorganic core was a frequent phenomenon in individual particles (diameters > 100 nm)
371 collected over the North China Plain (Li et al., 2021a). To assess the potential effects of inorganic compounds on the phase
372 state of ambient particles, we perform a sensitivity calculation (case C, Table 1) assuming that the organic and inorganic
373 compounds are internally mixed in one phase. In this case the water absorbed by inorganic species can lower the particle
374 viscosity relative to the organic fraction alone. Figure 10b shows that the water associated with inorganic species can
375 significantly lower the viscosity over most areas of China, with the liquid frequency increased by 15 – 45 % in the southeast,
376 and 5 – 15 % in some areas of the northeast. The effects over dry lands in the northwestern China are relatively small.
377 Previous studies showed that at such mixing condition with one phase, on one hand, it is expected that the inorganic salts that
378 often have lower T_g compared to SOA compounds would further lower the particle viscosity (Dette and Koop, 2015). On the
379 other hand, the presence of divalent inorganic ions could increase the viscosity of mixed organic-inorganic particles,
380 enabling a humidity-dependent gel phase transition through cooperative ion-molecule interactions (Richards et al., 2020).
381 For complex mixtures of primary OA, SOA and inorganics, it was found that three distinct phases could occur (Huang et al.,
382 2021). The impacts of the mixing state of organic and inorganic compounds on the phase state of multicomponent particles
383 in ambient air warrant further investigations in future studies (Lilek and Zuend, 2022; Schervish and Shiraiwa, 2023).

384 **4 Conclusions**

385 We previously developed a new parameterization predicting the glass transition temperature of an organic compound as a
386 function of its volatility (Li et al., 2020). Based on this new parameterization, we use the WRF-Chem model and simulate the
387 T_g and viscosity of SOA particles over China in summer of 2018. This is the first time that spatial and temporal variations in
388 the SOA phase state over China are investigated on a regional scale. The main conclusions are summarized below.

389 (1) Simulations show that T_g values of dry SOA ($T_{g,org}$) range from ~287 K to 305 K over most areas of China at the surface,
390 consistent with our previous simulated results based on a global transport model (Shiraiwa et al., 2017). The $T_{g,org}$ is higher
391 in the northwestern China than the southeastern China. This geospatial variation in $T_{g,org}$ is related to the simulated SOA
392 volatility distributions that SOA particles in northwestern China have relatively low volatilities.

393 (2) Considering the water uptake by SOA particles, the SOA viscosity also shows a prominent geospatial gradient that highly
394 viscous or solid SOA particles are mainly found in the northwestern China. The frequency of liquid SOA particles in most

395 areas with the latitude higher than 30°N is less than 20 %. A very large spatial variation in SOA phase state over the
396 Qinghai-Tibet Plateau was found and we recommend measurements in ambient particle phase state to be conducted over this
397 area, one of the most sensitive regions to climate change.

398 (3) The average volatility (C^*) and $T_{g,org}$ of the simulated SOA agree well with the values estimated from ambient
399 measurements of OOA volatilities at the IAP site in Beijing, where ELVOCs were not determined in the observed OOA (Xu
400 et al., 2019). The sensitivity simulation considering the formation of ELVOCs shows that compared to the base simulation,
401 the frequency of a liquid phase state does not change in most areas of the northern China. In some areas of the southeastern
402 China the SOA particles become more viscous with the percent time that a SOA particle is in the liquid phase state decreases
403 by up to 12 %. It needs more field volatility measurements to evaluate the effects of ELVOCs on OA phase state estimations
404 over China.

405 (4) Differed from the base simulation that SOA components are assumed to be phase separated from inorganic compounds in
406 particles, we conduct a sensitivity simulation assuming that the organic and inorganic compounds are internally mixed in one
407 phase. We show that the water absorbed by inorganic species has a significant impact lowering the simulated viscosity over
408 the southeastern China, with the liquid frequency increased by 15 – 45 %. Future work should consider the effects of the
409 mixing state of organic and inorganic compounds on the prediction of the phase state of multicomponent particles in ambient
410 air.

411 (5) The mixing timescale of organic molecules in 200 nm SOA particles is calculated based on the simulated particle
412 viscosity and the bulk diffusion coefficients of organic molecules. Calculations show that at the surface and at 500 hPa, the
413 percent time of τ_{mix} longer than 1 h is $> \sim 70\%$ in the northwest of the “Hu Huanyong Line”. The implication of this result is
414 that when the τ_{mix} values are greater than roughly 1 h, which is longer than the typical time step in CTMs, the instantaneous
415 equilibrium partitioning usually assumed in SOA formation simulations is subject to be re-evaluated. We recommend to test
416 the effects of kinetic partitioning considering the bulk diffusion in viscous particles on the prediction of SOA mass
417 concentrations and size distributions over the areas with long mixing timescale of organic molecules.

418

419 *Data availability.* The simulation data in this study are available upon request from the corresponding author
420 (liying-iap@mail.iap.ac.cn).

421 *Supplement.* The supplement related to this article is available on-line.

422 *Author contributions.* YL and MS designed the research. ZZ, HR, and YQ performed the WRF-Chem modeling. ZZ, YL,
423 and HR analyzed the simulation data. WZ, WX, WH, and YS provided observation data. YL and ZZ wrote the manuscript.
424 ZZ, YL, and HR wrote the supplement. All authors discussed the results and contributed to the article editing.

425 *Competing interests.* At least one of the (co-)authors is a member of the editorial board of Atmospheric Chemistry and
426 Physics. The peer-review process was guided by an independent editor, and the authors have also no other competing
427 interests to declare.

428 *Acknowledgements.* This work was supported by the National Natural Science Foundation of China (grant no. 42075110 and
429 42330605) and the National Key Research and Development Program of China (grant no. 2023YFC3710100). The authors
430 thank Qi Chen at the Peking University and Bin Zhao at the Tsinghua University for insightful suggestions on SOA volatility
431 simulations in this work. MS thanks U.S. National Science Foundation for funding (AGS- 2246502).

432 *Financial support.* This work was supported by the National Natural Science Foundation of China (grant no. 42075110).

433 **References**

- 434 Abbatt, J. P. D., Lee, A. K. Y., and Thornton, J. A.: Quantifying trace gas uptake to tropospheric aerosol: recent advances and
435 remaining challenges, *Chem. Soc. Rev.*, 41, 6555-6581, <https://doi.org/10.1039/C2CS35052A>, 2012.
- 436 Ahmadov, R., Mckeen, S. A., Robinson, A. L., Bahreini, R., Middlebrook, A. M., De Gouw, J. A., Meagher, J., Hsie, E. Y.,
437 Edgerton, E., Shaw, S., and Trainer, M.: A volatility basis set model for summertime secondary organic aerosols over
438 the eastern United States in 2006, *J. Geophys. Res.: Atmos.*, 117, <https://doi.org/10.1029/2011JD016831>, 2012.
- 439 Angell, C. A.: Relaxation in liquids, polymers and plastic crystals — strong/fragile patterns and problems, *J. Non-Cryst.*
440 *Solids*, 131-133, 13-31, [https://doi.org/10.1016/0022-3093\(91\)90266-9](https://doi.org/10.1016/0022-3093(91)90266-9), 1991.
- 441 Baboornian, V. J., Crescenzo, G. V., Huang, Y., Mahrt, F., Shiraiwa, M., Bertram, A. K., and Nizkorodov, S. A.: Sunlight can
442 convert atmospheric aerosols into a glassy solid state and modify their environmental impacts, *P. Natl. Acad. Sci. USA*,
443 119, e2208121119, <https://doi.org/10.1073/pnas.2208121119>, 2022.
- 444 Champion, W. M., Rothfuss, N. E., Petters, M. D., and Grieshop, A. P.: Volatility and viscosity are correlated in terpene
445 secondary organic aerosol formed in a flow reactor, *Environ. Sci. Technol. Lett.*, 6, 513-519,
446 <https://doi.org/10.1021/acs.estlett.9b00412>, 2019.
- 447 Chang, X., Zhao, B., Zheng, H., Wang, S., Cai, S., Guo, F., Gui, P., Huang, G., Wu, D., Han, L., Xing, J., Man, H., Hu, R.,
448 Liang, C., Xu, Q., Qiu, X., Ding, D., Liu, K., Han, R., Robinson, A. L., and Donahue, N. M.: Full-volatility emission
449 framework corrects missing and underestimated secondary organic aerosol sources, *One Earth*, 5, 403-412,
450 <https://doi.org/10.1016/j.oneear.2022.03.015>, 2022.
- 451 Dalton, A. B. and Nizkorodov, S. A.: Photochemical degradation of 4-nitrocatechol and 2,4-dinitrophenol in a sugar-glass
452 secondary organic aerosol surrogate, *Environ. Sci. Technol.*, 55, 14586-14594, <https://doi.org/10.1021/acs.est.1c04975>,
453 2021.
- 454 DeRieux, W. S. W., Li, Y., Lin, P., Laskin, J., Laskin, A., Bertram, A. K., Nizkorodov, S. A., and Shiraiwa, M.: Predicting the
455 glass transition temperature and viscosity of secondary organic material using molecular composition, *Atmos. Chem.*
456 *Phys.*, 18, 6331-6351, <https://doi.org/10.5194/acp-18-6331-2018>, 2018.
- 457 Dette, H. P. and Koop, T.: Glass formation processes in mixed inorganic/organic aerosol particles, *J. Phys. Chem. A*, 119,
458 4552-4561, <https://doi.org/10.1021/jp5106967>, 2015.
- 459 Dette, H. P., Qi, M., Schröder, D. C., Godt, A., and Koop, T.: Glass-forming properties of 3-methylbutane-1,2,3-tricarboxylic
460 acid and its mixtures with water and pinonic acid, *J. Phys. Chem. A*, 118, 7024-7033,
461 <https://doi.org/10.1021/jp505910w>, 2014.
- 462 Donahue, N., Robinson, A., Stanier, C., and Pandis, S.: Coupled partitioning, dilution, and chemical aging of semivolatile
463 organics, *Environ. Sci. Technol.*, 40, 2635-2643, <https://doi.org/10.1021/es052297c>, 2006.
- 464 Donahue, N. M., Epstein, S. A., Pandis, S. N., and Robinson, A. L.: A two-dimensional volatility basis set: 1. organic-aerosol

465 mixing thermodynamics, *Atmos. Chem. Phys.*, 11, 3303-3318, <https://doi.org/10.5194/acp-11-3303-2011>, 2011.

466 Donahue, N. M., Kroll, J. H., Pandis, S. N., and Robinson, A. L.: A two-dimensional volatility basis set – Part 2: Diagnostics
467 of organic-aerosol evolution, *Atmos. Chem. Phys.*, 12, 615-634, <https://doi.org/10.5194/acp-12-615-2012>, 2012.

468 Dong, W., Lin, Y., Wright, J. S., Ming, Y., Xie, Y., Wang, B., Luo, Y., Huang, W., Huang, J., Wang, L., Tian, L., Peng, Y., and
469 Xu, F.: Summer rainfall over the southwestern Tibetan Plateau controlled by deep convection over the Indian
470 subcontinent, *Nat. Commun.*, 7, 10925, <https://doi.org/10.1038/ncomms10925>, 2016.

471 Duplissy, J., Decarlo, P. F., Dommen, J., Alfarra, M. R., Metzger, A., Barmapadimos, I., Prevot, A. S. H., Weingartner, E.,
472 Tritscher, T., Gysel, M., Aiken, A. C., Jimenez, J. L., Canagaratna, M. R., Worsnop, D. R., Collins, D. R., Tomlinson, J.,
473 and Baltensperger, U.: Relating hygroscopicity and composition of organic aerosol particulate matter, *Atmos. Chem.*
474 *Phys.*, 11, 1155-1165, <https://doi.org/10.5194/acp-11-1155-2011>, 2011.

475 Einstein, A.: Über die von der molekularkinetischen Theorie der Wärme geforderte Bewegung von in ruhenden Flüssigkeiten
476 suspendierten Teilchen, 322, 549-560, <https://doi.org/10.1002/andp.19053220806>, 1905.

477 Emmons, L. K., Walters, S., Hess, P. G., Lamarque, J. F., Pfister, G. G., Fillmore, D., Granier, C., Guenther, A., Kinnison, D.,
478 Laepple, T., Orlando, J., Tie, X., Tyndall, G., Wiedinmyer, C., Baughcum, S. L., and Kloster, S.: Description and
479 evaluation of the model for ozone and related chemical tracers, version 4 (MOZART-4), *Geosci. Model Dev.*, 3, 43-67,
480 <https://doi.org/10.5194/gmd-3-43-2010>, 2010.

481 Epstein, S. A., Riipinen, I., and Donahue, N. M.: A semiempirical correlation between enthalpy of vaporization and
482 saturation concentration for organic aerosol, *Environ. Sci. Technol.*, 44, 743-748, <https://doi.org/10.1021/es902497z>,
483 2010.

484 Evoy, E., Kamal, S., Patey, G. N., Martin, S. T., and Bertram, A. K.: Unified description of diffusion coefficients from small
485 to large molecules in organic–water mixtures, *J. Phys. Chem. A*, 124, 2301-2308,
486 <https://doi.org/10.1021/acs.jpca.9b11271>, 2020.

487 Evoy, E., Maclean, A. M., Rovelli, G., Li, Y., Tsimpidi, A. P., Karydis, V. A., Kamal, S., Lelieveld, J., Shiraiwa, M., Reid, J.
488 P., and Bertram, A. K.: Predictions of diffusion rates of large organic molecules in secondary organic aerosols using the
489 Stokes–Einstein and fractional Stokes–Einstein relations, *Atmos. Chem. Phys.*, 19, 10073-10085,
490 <https://doi.org/10.5194/acp-19-10073-2019>, 2019.

491 Fast, J. D., Gustafson Jr, W. I., Easter, R. C., Zaveri, R. A., Barnard, J. C., Chapman, E. G., Grell, G. A., and Peckham, S. E.:
492 Evolution of ozone, particulates, and aerosol direct radiative forcing in the vicinity of Houston using a fully coupled
493 meteorology-chemistry-aerosol model, *J. Geophys. Res.: Atmos.*, 111, <https://doi.org/10.1029/2005JD006721>, 2006.

494 Feng, T., Wang, Y., Hu, W., Zhu, M., Song, W., Chen, W., Sang, Y., Fang, Z., Deng, W., Fang, H., Yu, X., Wu, C., Yuan, B.,
495 Huang, S., Shao, M., Huang, X., He, L., Lee, Y. R., Huey, L. G., Canonaco, F., Prevot, A. S. H., and Wang, X.: Impact
496 of aging on the sources, volatility, and viscosity of organic aerosols in Chinese outflows, *Atmos. Chem. Phys.*, 23,
497 611-636, <https://doi.org/10.5194/acp-23-611-2023>, 2023.

498 Fröhlich, R., Cubison, M. J., Slowik, J. G., Bukowiecki, N., Prévôt, A. S. H., Baltensperger, U., Schneider, J., Kimmel, J. R.,
499 Gonin, M., Rohner, U., Worsnop, D. R., and Jayne, J. T.: The ToF-ACSM: a portable aerosol chemical speciation
500 monitor with TOFMS detection, *Atmos. Meas. Tech.*, 6, 3225-3241, <https://doi.org/10.5194/amt-6-3225-2013>, 2013.

501 Galeazzo, T. and Shiraiwa, M.: Predicting glass transition temperature and melting point of organic compounds via machine
502 learning and molecular embeddings, *Environ. Sci.: Atmos.*, <https://doi.org/10.1039/D1EA00090J>, 2022.

503 Gervasi, N. R., Topping, D. O., and Zuend, A.: A predictive group-contribution model for the viscosity of aqueous organic
504 aerosol, *Atmos. Chem. Phys.*, 20, 2987-3008, <https://doi.org/10.5194/acp-20-2987-2020>, 2020.

505 Gordon, M. and Taylor, J. S.: Ideal copolymers and the second-order transitions of synthetic rubbers. i. non-crystalline
506 copolymers, *J. Appl. Chem.*, 2, 493-500, <https://doi.org/10.1002/jctb.5010020901>, 1952.

507 Grell, G. A., Peckham, S. E., Schmitz, R., Mckeen, S. A., Frost, G., Skamarock, W. C., and Eder, B.: Fully coupled “online”
508 chemistry within the WRF model, *Atmos. Environ.*, 39, 6957-6975, <https://doi.org/10.1016/j.atmosenv.2005.04.027>,
509 2005.

510 Guenther, A. B., Jiang, X., Heald, C. L., Sakulyanontvittaya, T., Duhl, T., Emmons, L. K., and Wang, X.: The Model of
511 Emissions of Gases and Aerosols from Nature version 2.1 (MEGAN2.1): an extended and updated framework for

512 modeling biogenic emissions, *Geosci. Model Dev.*, 5, 1471-1492, <https://doi.org/10.5194/gmd-5-1471-2012>, 2012.

513 Gunthe, S. S., King, S. M., Rose, D., Chen, Q., Roldin, P., Farmer, D. K., Jimenez, J. L., Artaxo, P., Andreae, M. O., Martin,
514 S. T., and Pöschl, U.: Cloud condensation nuclei in pristine tropical rainforest air of Amazonia: size-resolved
515 measurements and modeling of atmospheric aerosol composition and CCN activity, *Atmos. Chem. Phys.*, 9, 7551-7575,
516 <https://doi.org/10.5194/acp-9-7551-2009>, 2009.

517 He, Y., Akherati, A., Nah, T., Ng, N. L., Garofalo, L. A., Farmer, D. K., Shiraiwa, M., Zaveri, R. A., Cappa, C. D., Pierce, J.
518 R., and Jathar, S. H.: Particle size distribution dynamics can help constrain the phase state of secondary organic aerosol,
519 *Environ. Sci. Technol.*, 55, 1466-1476, <https://doi.org/10.1021/acs.est.0c05796>, 2021.

520 Hu, H.: The distribution of China's population, *Acta Geogr. Sin.*, 2, 33-73, <https://doi.org/10.11821/xb193502002>, 1935.

521 Huang, R., Zhang, Z., Huang, G., and Ren, B.: Characteristics of the water vapor transport in east Asian monsoon region and
522 its differences from that of south Asian monsoon region in summer, *Chinese J. Atmospheric Sci.*, 22, 368-379,
523 <https://doi.org/10.3878/j.issn.1006-9895.2003.19204>, 1998.

524 Huang, Y., Mahrt, F., Xu, S., Shiraiwa, M., Zuend, A., and Bertram, A. K.: Coexistence of three liquid phases in individual
525 atmospheric aerosol particles, *P. Natl. Acad. Sci. USA*, 118, e2102512118, <https://doi.org/10.1073/pnas.2102512118>,
526 2021.

527 Jathar, S. H., Cappa, C. D., He, Y., Pierce, J. R., Chuang, W., Bilsback, K. R., Seinfeld, J. H., Zaveri, R. A., and Shrivastava,
528 M.: A computationally efficient model to represent the chemistry, thermodynamics, and microphysics of secondary
529 organic aerosols (simpleSOM): model development and application to α -pinene SOA, *Environ. Sci.: Atmos.*, 1, 372-394,
530 <https://doi.org/10.1039/D1EA00014D>, 2021.

531 Jimenez, J. L., Canagaratna, M. R., Donahue, N. M., Prevot, A. S. H., Zhang, Q., Kroll, J. H., Decarlo, P. F., Allan, J. D., Coe,
532 H., Ng, N. L., Aiken, A. C., Docherty, K. S., Ulbrich, I. M., Grieshop, A. P., Robinson, A. L., Duplissy, J., Smith, J. D.,
533 Wilson, K. R., Lanz, V. A., Hueglin, C., Sun, Y. L., Tian, J., Laaksonen, A., Raatikainen, T., Rautiainen, J., Vaattovaara,
534 P., Ehn, M., Kulmala, M., Tomlinson, J. M., Collins, D. R., Cubison, M. J., Dunlea, J., Huffman, J. A., Onasch, T. B.,
535 Alfarra, M. R., Williams, P. I., Bower, K., Kondo, Y., Schneider, J., Drewnick, F., Borrmann, S., Weimer, S., Demerjian,
536 K., Salcedo, D., Cottrell, L., Griffin, R., Takami, A., Miyoshi, T., Hatakeyama, S., Shimono, A., Sun, J. Y., Zhang, Y. M.,
537 Dzepina, K., Kimmel, J. R., Sueper, D., Jayne, J. T., Herndon, S. C., Trimborn, A. M., Williams, L. R., Wood, E. C.,
538 Middlebrook, A. M., Kolb, C. E., Baltensperger, U., and Worsnop, D. R.: Evolution of organic aerosols in the
539 atmosphere, *Science*, 326, 1525, <https://doi.org/10.1126/science.1180353>, 2009.

540 Kanakidou, M., Seinfeld, J. H., Pandis, S. N., Barnes, I., Dentener, F. J., Facchini, M. C., Van Dingenen, R., Ervens, B.,
541 Nenes, A., Nielsen, C. J., Swietlicki, E., Putaud, J. P., Balkanski, Y., Fuzzi, S., Horth, J., Moortgat, G. K., Winterhalter,
542 R., Myhre, C. E. L., Tsigaridis, K., Vignati, E., Stephanou, E. G., and Wilson, J.: Organic aerosol and global climate
543 modelling: a review, *Atmos. Chem. Phys.*, 5, 1053-1123, <https://doi.org/10.5194/acp-5-1053-2005>, 2005.

544 Karnezi, E., Riipinen, I., and Pandis, S. N.: Measuring the atmospheric organic aerosol volatility distribution: a theoretical
545 analysis, *Atmos. Meas. Tech.*, 7, 2953-2965, <https://doi.org/10.5194/amt-7-2953-2014>, 2014.

546 Knopf, D. A. and Alpert, P. A.: Atmospheric ice nucleation, *Nat. Rev. Phys.*, 5, 203-217,
547 <https://doi.org/10.1038/s42254-023-00570-7>, 2023.

548 Knote, C., Hodzic, A., and Jimenez, J. L.: The effect of dry and wet deposition of condensable vapors on secondary organic
549 aerosols concentrations over the continental US, *Atmos. Chem. Phys.*, 15, 1-18, <https://doi.org/10.5194/acp-15-1-2015>,
550 2015.

551 Kohl, I., Bachmann, L., Hallbrucker, A., Mayer, E., and Loerting, T.: Liquid-like relaxation in hyperquenched water at ≤ 140
552 K, *Phys. Chem. Chem. Phys.*, 7, 3210-3220, <https://doi.org/10.1039/B507651J>, 2005.

553 Koop, T., Bookhold, J., Shiraiwa, M., and Pöschl, U.: Glass transition and phase state of organic compounds: dependency on
554 molecular properties and implications for secondary organic aerosols in the atmosphere, *Phys. Chem. Chem. Phys.*, 13,
555 19238-19255, <https://doi.org/10.1039/C1CP22617G>, 2011.

556 Kuwata, M. and Martin, S. T.: Phase of atmospheric secondary organic material affects its reactivity, *P. Natl. Acad. Sci. USA*,
557 109, 17354-17359, <https://doi.org/10.1073/pnas.1209071109>, 2012.

558 Lane, T. E., Donahue, N. M., and Pandis, S. N.: Effect of NO_x on secondary organic aerosol concentrations, *Environ. Sci.*

Technol., 42, 6022-6027, <https://doi.org/10.1021/es703225a>, 2008a.

Lane, T. E., Donahue, N. M., and Pandis, S. N.: Simulating secondary organic aerosol formation using the volatility basis-set approach in a chemical transport model, *Atmos. Environ.*, 42, 7439-7451, <https://doi.org/10.1016/j.atmosenv.2008.06.026>, 2008b.

Li, J., Han, Z., Wu, J., Tao, J., Li, J., Sun, Y., Liang, L., Liang, M., and Wang, Q. G.: Secondary organic aerosol formation and source contributions over east China in summertime, *Environ. Pollut.*, 306, 119383, <https://doi.org/10.1016/j.envpol.2022.119383>, 2022.

Li, M., Zhang, Q., Kurokawa, J. I., Woo, J. H., He, K., Lu, Z., Ohara, T., Song, Y., Streets, D. G., Carmichael, G. R., Cheng, Y., Hong, C., Huo, H., Jiang, X., Kang, S., Liu, F., Su, H., and Zheng, B.: MIX: a mosaic Asian anthropogenic emission inventory under the international collaboration framework of the MICS-Asia and HTAP, *Atmos. Chem. Phys.*, 17, 935-963, <https://doi.org/10.5194/acp-17-935-2017>, 2017.

Li, W., Liu, L., Zhang, J., Xu, L., Wang, Y., Sun, Y., and Shi, Z.: Microscopic evidence for phase separation of organic species and inorganic salts in fine ambient aerosol particles, *Environ. Sci. Technol.*, 55, 2234-2242, <https://doi.org/10.1021/acs.est.0c02333>, 2021a.

Li, Y. and Shiraiwa, M.: Timescales of secondary organic aerosols to reach equilibrium at various temperatures and relative humidities, *Atmos. Chem. Phys.*, 19, 5959-5971, <https://doi.org/10.5194/acp-19-5959-2019>, 2019.

Li, Y., An, J., and Gultepe, I.: Effects of additional HONO sources on visibility over the North China Plain, *Adv. Atmos. Sci.*, 31, 1221-1232, <https://doi.org/10.1007/s00376-014-4019-1>, 2014.

Li, Y., Carlton, A. G., and Shiraiwa, M.: Diurnal and seasonal variations in the phase state of secondary organic aerosol material over the contiguous US simulated in CMAQ, *ACS Earth Space Chem.*, 5, 1971-1982, <https://doi.org/10.1021/acsearthspacechem.1c00094>, 2021b.

Li, Y., Day, D. A., Stark, H., Jimenez, J. L., and Shiraiwa, M.: Predictions of the glass transition temperature and viscosity of organic aerosols from volatility distributions, *Atmos. Chem. Phys.*, 20, 8103-8122, <https://doi.org/10.5194/acp-20-8103-2020>, 2020.

Li, Y., An, J., Min, M., Zhang, W., Wang, F., and Xie, P.: Impacts of HONO sources on the air quality in Beijing, Tianjin and Hebei Province of China, *Atmos. Environ.*, 45, 4735-4744, <https://doi.org/10.1016/j.atmosenv.2011.04.086>, 2011.

Li, Y., An, J., Kajino, M., Gultepe, I., Chen, Y., Song, T., and Xin, J.: Impacts of additional HONO sources on O₃ and PM_{2.5} chemical coupling and control strategies in the Beijing–Tianjin–Hebei region of China, *Tellus B*, 67, 23930, <https://doi.org/10.3402/tellusb.v67.23930>, 2015.

Li, Z., Xu, W., Zhou, W., Lei, L., Sun, J., You, B., Wang, Z., and Sun, Y.: Insights into the compositional differences of PM₁ and PM_{2.5} from aerosol mass spectrometer measurements in Beijing, China, *Atmos. Environ.*, 301, 119709, <https://doi.org/10.1016/j.atmosenv.2023.119709>, 2023.

Lilek, J. and Zuend, A.: A predictive viscosity model for aqueous electrolytes and mixed organic–inorganic aerosol phases, *Atmos. Chem. Phys.*, 22, 3203-3233, <https://doi.org/10.5194/acp-22-3203-2022>, 2022.

Liu, P., Li, Y. J., Wang, Y., Bateman, A. P., Zhang, Y., Gong, Z., Bertram, A. K., and Martin, S. T.: Highly viscous states affect the browning of atmospheric organic particulate matter, *ACS Cent. Sci.*, 4, 207-215, <https://doi.org/10.1021/acscentsci.7b00452>, 2018.

Liu, Y., Wu, Z., Wang, Y., Xiao, Y., Gu, F., Zheng, J., Tan, T., Shang, D., Wu, Y., Zeng, L., Hu, M., Bateman, A. P., and Martin, S. T.: Submicrometer particles are in the liquid state during heavy haze episodes in the urban atmosphere of Beijing, China, *Environ. Sci. Technol. Lett.*, 4, 427-432, <https://doi.org/10.1021/acs.estlett.7b00352>, 2017.

Liu, Y., Wu, Z., Huang, X., Shen, H., Bai, Y., Qiao, K., Meng, X., Hu, W., Tang, M., and He, L.: Aerosol phase state and its link to chemical composition and liquid water content in a subtropical coastal megacity, *Environ. Sci. Technol.*, 53, 5027-5033, <https://doi.org/10.1021/acs.est.9b01196>, 2019.

Liu, Y., Meng, X., Wu, Z., Huang, D., Wang, H., Chen, J., Chen, J., Zong, T., Fang, X., Tan, T., Zhao, G., Chen, S., Zeng, L., Guo, S., Huang, X., He, L., Zeng, L., and Hu, M.: The particle phase state during the biomass burning events, *Sci. Total Environ.*, 792, 148035, <https://doi.org/10.1016/j.scitotenv.2021.148035>, 2021.

Maclean, A. M., Butenhoff, C. L., Grayson, J. W., Barsanti, K., Jimenez, J. L., and Bertram, A. K.: Mixing times of organic

606 molecules within secondary organic aerosol particles: a global planetary boundary layer perspective, *Atmos. Chem.*
607 *Phys.*, 17, 13037-13048, <https://doi.org/10.5194/acp-17-13037-2017>, 2017.

608 Maclean, A. M., Li, Y., Crescenzo, G. V., Smith, N. R., Karydis, V. A., Tsimpidi, A. P., Butenhoff, C. L., Faiola, C. L.,
609 Lelieveld, J., Nizkorodov, S. A., Shiraiwa, M., and Bertram, A. K.: Global distribution of the phase state and mixing
610 times within secondary organic aerosol particles in the troposphere based on room-temperature viscosity measurements,
611 *ACS Earth Space Chem.*, 5, 3458-3473, <https://doi.org/10.1021/acsearthspacechem.1c00296>, 2021.

612 Marshall, F. H., Berkemeier, T., Shiraiwa, M., Nandy, L., Ohm, P. B., Dutcher, C. S., and Reid, J. P.: Influence of particle
613 viscosity on mass transfer and heterogeneous ozonolysis kinetics in aqueous–sucrose–maleic acid aerosol, *Phys. Chem.*
614 *Chem. Phys.*, 20, 15560-15573, <https://doi.org/10.1039/C8CP01666F>, 2018.

615 Meng, X., Wu, Z., Guo, S., Wang, H., Liu, K., Zong, T., Liu, Y., Zhang, W., Zhang, Z., Chen, S., Zeng, L., Hallquist, M.,
616 Shuai, S., and Hu, M.: Humidity-dependent phase state of gasoline vehicle emission-related aerosols, *Environ. Sci.*
617 *Technol.*, 55, 832-841, <https://doi.org/10.1021/acs.est.0c05478>, 2021.

618 Miao, R., Chen, Q., Shrivastava, M., Chen, Y., Zhang, L., Hu, J., Zheng, Y., and Liao, K.: Process-based and
619 observation-constrained SOA simulations in China: the role of semivolatile and intermediate-volatility organic
620 compounds and OH levels, *Atmos. Chem. Phys.*, 21, 16183-16201, <https://doi.org/10.5194/acp-21-16183-2021>, 2021.

621 Mikhailov, E., Vlasenko, S., Martin, S. T., Koop, T., and Pöschl, U.: Amorphous and crystalline aerosol particles interacting
622 with water vapor: conceptual framework and experimental evidence for restructuring, phase transitions and kinetic
623 limitations, *Atmos. Chem. Phys.*, 9, 9491-9522, <https://doi.org/10.5194/acp-9-9491-2009>, 2009.

624 Murphy, B. N. and Pandis, S. N.: Simulating the formation of semivolatile primary and secondary organic aerosol in a
625 regional chemical transport model, *Environ. Sci. Technol.*, 43, 4722-4728, <https://doi.org/10.1021/es803168a>, 2009.

626 Pankow, J. F.: An absorption model of gas/particle partitioning of organic compounds in the atmosphere, *Atmos. Environ.*, 28,
627 185-188, [https://doi.org/10.1016/1352-2310\(94\)90093-0](https://doi.org/10.1016/1352-2310(94)90093-0), 1994.

628 Petters, M. D. and Kreidenweis, S. M.: A single parameter representation of hygroscopic growth and cloud condensation
629 nucleus activity, *Atmos. Chem. Phys.*, 7, 1961-1971, <https://doi.org/10.5194/acp-7-1961-2007>, 2007.

630 Pöschl, U. and Shiraiwa, M.: Multiphase chemistry at the atmosphere–biosphere interface influencing climate and public
631 health in the anthropocene, *Chem. Rev.*, 115, 4440-4475, <https://doi.org/10.1021/cr500487s>, 2015.

632 Preston, T. C. and Zuend, A.: Equilibration times in viscous and viscoelastic aerosol particles, *Environ. Sci.: Atmos.*,
633 <https://doi.org/10.1039/D2EA00065B>, 2022.

634 Price, H. C., Mattsson, J., and Murray, B. J.: Sucrose diffusion in aqueous solution, *Phys. Chem. Chem. Phys.*, 18,
635 19207-19216, <https://doi.org/10.1039/C6CP03238A>, 2016.

636 Qu, Y., Chen, Y., Liu, X., Zhang, J., Guo, Y., and An, J.: Seasonal effects of additional HONO sources and the heterogeneous
637 reactions of N₂O₅ on nitrate in the North China Plain, *Sci. Total Environ.*, 690, 97-107,
638 <https://doi.org/10.1016/j.scitotenv.2019.06.436>, 2019.

639 Rasool, Q. Z., Shrivastava, M., Liu, Y., Gaudet, B., and Zhao, B.: Modeling the Impact of the Organic Aerosol Phase State
640 on Multiphase OH Reactive Uptake Kinetics and the Resultant Heterogeneous Oxidation Timescale of Organic Aerosol
641 in the Amazon Rainforest, *ACS Earth Space Chem.*, <https://doi.org/10.1021/acsearthspacechem.2c00366>, 2023.

642 Rasool, Q. Z., Shrivastava, M., Octaviani, M., Zhao, B., Gaudet, B., and Liu, Y.: Modeling volatility-based aerosol phase
643 state predictions in the Amazon Rainforest, *ACS Earth Space Chem.*, 5, 2910-2924,
644 <https://doi.org/10.1021/acsearthspacechem.1c00255>, 2021.

645 Reid, J. P., Bertram, A. K., Topping, D. O., Laskin, A., Martin, S. T., Petters, M. D., Pope, F. D., and Rovelli, G.: The
646 viscosity of atmospherically relevant organic particles, *Nat. Commun.*, 9, 956,
647 <https://doi.org/10.1038/s41467-018-03027-z>, 2018.

648 Richards, D. S., Trobaugh, K. L., Hajek-Herrera, J., Price, C. L., Sheldon, C. S., Davies, J. F., and Davis, R. D.: Ion-molecule
649 interactions enable unexpected phase transitions in organic-inorganic aerosol, *Sci. Adv.*, 6, eabb5643,
650 <https://doi.org/10.1126/sciadv.abb5643>, 2020.

651 Riipinen, I., Pierce, J. R., Donahue, N. M., and Pandis, S. N.: Equilibration time scales of organic aerosol inside
652 thermodenuders: Evaporation kinetics versus thermodynamics, *Atmos. Environ.*, 44, 597-607,

653 <https://doi.org/10.1016/j.atmosenv.2009.11.022>, 2010.

654 Roldin, P., Eriksson, A. C., Nordin, E. Z., Hermansson, E., Mogensen, D., Rusanen, A., Boy, M., Swietlicki, E.,
655 Svenningsson, B., Zelenyuk, A., and Pagels, J.: Modelling non-equilibrium secondary organic aerosol formation and
656 evaporation with the aerosol dynamics, gas- and particle-phase chemistry kinetic multilayer model ADCHAM, *Atmos.*
657 *Chem. Phys.*, 14, 7953-7993, <https://doi.org/10.5194/acp-14-7953-2014>, 2014.

658 Rothfuss, N. E. and Petters, M. D.: Influence of functional groups on the viscosity of organic aerosol, *Environ. Sci. Technol.*,
659 51, 271-279, <https://doi.org/10.1021/acs.est.6b04478>, 2017.

660 Schervish, M. and Shiraiwa, M.: Impact of phase state and non-ideal mixing on equilibration timescales of secondary organic
661 aerosol partitioning, *Atmos. Chem. Phys.*, 23, 221-233, <https://doi.org/10.5194/acp-23-221-2023>, 2023.

662 Schmedding, R., Rasool, Q. Z., Zhang, Y., Pye, H. O. T., Zhang, H., Chen, Y., Surratt, J. D., Lopez-Hilfiker, F. D., Thornton,
663 J. A., Goldstein, A. H., and Vizuete, W.: Predicting secondary organic aerosol phase state and viscosity and its effect on
664 multiphase chemistry in a regional-scale air quality model, *Atmos. Chem. Phys.*, 20, 8201-8225,
665 <https://doi.org/10.5194/acp-20-8201-2020>, 2020.

666 Seinfeld, J. H. and Pandis, S. N.: Atmospheric chemistry and physics: from air pollution to climate change, John Wiley &
667 Sons, 2016.

668 Shiraiwa, M. and Pöschl, U.: Mass accommodation and gas-particle partitioning in secondary organic aerosols: dependence
669 on diffusivity, volatility, particle-phase reactions, and penetration depth, *Atmos. Chem. Phys.*, 21, 1565-1580,
670 <https://doi.org/10.5194/acp-21-1565-2021>, 2021.

671 Shiraiwa, M. and Seinfeld, J. H.: Equilibration timescale of atmospheric secondary organic aerosol partitioning, *Geophys.*
672 *Res. Lett.*, 39, <https://doi.org/10.1029/2012GL054008>, 2012.

673 Shiraiwa, M., Yee, L. D., Schilling, K. A., Loza, C. L., Craven, J. S., Zuend, A., Ziemann, P. J., and Seinfeld, J. H.: Size
674 distribution dynamics reveal particle-phase chemistry in organic aerosol formation, *P. Natl. Acad. Sci. USA*, 110, 11746,
675 <https://doi.org/10.1073/pnas.1307501110>, 2013.

676 Shiraiwa, M., Li, Y., Tsimpidi, A. P., Karydis, V. A., Berkemeier, T., Pandis, S. N., Lelieveld, J., Koop, T., and Pöschl, U.:
677 Global distribution of particle phase state in atmospheric secondary organic aerosols, *Nat. Commun.*, 8, 15002,
678 <https://doi.org/10.1038/ncomms15002>, 2017.

679 Shrivastava, M., Fast, J., Easter, R., Gustafson Jr, W. I., Zaveri, R. A., Jimenez, J. L., Saide, P., and Hodzic, A.: Modeling
680 organic aerosols in a megacity: comparison of simple and complex representations of the volatility basis set approach,
681 *Atmos. Chem. Phys.*, 11, 6639-6662, <https://doi.org/10.5194/acp-11-6639-2011>, 2011.

682 Shrivastava, M., Rasool, Q. Z., Zhao, B., Octaviani, M., Zaveri, R. A., Zelenyuk, A., Gaudet, B., Liu, Y., Shilling, J. E.,
683 Schneider, J., Schulz, C., Zöger, M., Martin, S. T., Ye, J., Guenther, A., Souza, R. F., Wendisch, M., and Pöschl, U.:
684 Tight coupling of surface and in-plant biochemistry and convection governs key fine particulate components over the
685 Amazon Rainforest, *ACS Earth Space Chem.*, 6, 380-390, <https://doi.org/10.1021/acsearthspacechem.1c00356>, 2022.

686 Shrivastava, M., Cappa, C. D., Fan, J., Goldstein, A. H., Guenther, A. B., Jimenez, J. L., Kuang, C., Laskin, A., Martin, S. T.,
687 Ng, N. L., Petaja, T., Pierce, J. R., Rasch, P. J., Roldin, P., Seinfeld, J. H., Shilling, J., Smith, J. N., Thornton, J. A.,
688 Volkamer, R., Wang, J., Worsnop, D. R., Zaveri, R. A., Zelenyuk, A., and Zhang, Q.: Recent advances in understanding
689 secondary organic aerosol: implications for global climate forcing, *Rev. Geophys.*, 55, 509-559,
690 <https://doi.org/10.1002/2016RG000540>, 2017.

691 Song, M., Jeong, R., Kim, D., Qiu, Y., Meng, X., Wu, Z., Zuend, A., Ha, Y., Kim, C., Kim, H., Gaikwad, S., Jang, K.-S., Lee,
692 J. Y., and Ahn, J.: Comparison of phase states of PM_{2.5} over megacities, Seoul and Beijing, and their implications on
693 particle size distribution, *Environ. Sci. Technol.*, <https://doi.org/10.1021/acs.est.2c06377>, 2022.

694 Song, Y. C., Haddrell, A. E., Bzdek, B. R., Reid, J. P., Bannan, T., Topping, D. O., Percival, C., and Cai, C.: Measurements
695 and predictions of binary component aerosol particle viscosity, *J. Phys. Chem. A*, 120, 8123-8137,
696 <https://doi.org/10.1021/acs.jpca.6b07835>, 2016.

697 Tan, W., Li, C., Liu, Y., Meng, X., Wu, Z., Kang, L., and Zhu, T.: Potential of polarization lidar to profile the urban aerosol
698 phase state during haze episodes, *Environ. Sci. Technol. Lett.*, 7, 54-59, <https://doi.org/10.1021/acs.estlett.9b00695>,
699 2020.

700 Tong, Y.-K., Liu, Y., Meng, X., Wang, J., Zhao, D., Wu, Z., and Ye, A.: Relative humidity-dependent viscosity of single quasi
701 aerosol particle and possible implications for atmospheric aerosol chemistry, *Phys. Chem. Chem. Phys.*,
702 <https://doi.org/10.1039/D2CP00740A>, 2022.

703 Wu, Z. J., Poulain, L., Henning, S., Dieckmann, K., Birmili, W., Merkel, M., Van Pinxteren, D., Spindler, G., Müller, K.,
704 Stratmann, F., Herrmann, H., and Wiedensohler, A.: Relating particle hygroscopicity and CCN activity to chemical
705 composition during the HCCT-2010 field campaign, *Atmos. Chem. Phys.*, 13, 7983-7996,
706 <https://doi.org/10.5194/acp-13-7983-2013>, 2013.

707 Xu, W., Xie, C., Karnezi, E., Zhang, Q., Wang, J., Pandis, S. N., Ge, X., Zhang, J., An, J., Wang, Q., Zhao, J., Du, W., Qiu, Y.,
708 Zhou, W., He, Y., Li, Y., Li, J., Fu, P., Wang, Z., Worsnop, D. R., and Sun, Y.: Summertime aerosol volatility
709 measurements in Beijing, China, *Atmos. Chem. Phys.*, 19, 10205-10216, <https://doi.org/10.5194/acp-19-10205-2019>,
710 2019.

711 Zaveri, R. A., Easter, R. C., Fast, J. D., and Peters, L. K.: Model for Simulating Aerosol Interactions and Chemistry
712 (MOSAIC), *J. Geophys. Res.: Atmos.*, 113, <https://doi.org/10.1029/2007JD008782>, 2008.

713 Zaveri, R. A., Easter, R. C., Shilling, J. E., and Seinfeld, J. H.: Modeling kinetic partitioning of secondary organic aerosol
714 and size distribution dynamics: representing effects of volatility, phase state, and particle-phase reaction, *Atmos. Chem.*
715 *Phys.*, 14, 5153-5181, <https://doi.org/10.5194/acp-14-5153-2014>, 2014.

716 Zaveri, R. A., Shilling, J. E., Zelenyuk, A., Zawadowicz, M. A., Suski, K., China, S., Bell, D. M., Veghte, D., and Laskin, A.:
717 Particle-phase diffusion modulates partitioning of semivolatile organic compounds to aged secondary organic aerosol,
718 *Environ. Sci. Technol.*, 54, 2595-2605, <https://doi.org/10.1021/acs.est.9b05514>, 2020.

719 Zaveri, R. A., Wang, J., Fan, J., Zhang, Y., Shilling, J. E., Zelenyuk, A., Mei, F., Newsom, R., Pekour, M., Tomlinson, J.,
720 Comstock, J. M., Shrivastava, M., Fortner, E., Machado, L. a. T., Artaxo, P., and Martin, S. T.: Rapid growth of
721 anthropogenic organic nanoparticles greatly alters cloud life cycle in the Amazon rainforest, *Sci. Adv.*, 8, eabj0329,
722 <https://doi.org/10.1126/sciadv.abj0329>, 2022.

723 Zaveri, R. A., Shilling, J. E., Zelenyuk, A., Liu, J., Bell, D. M., D'ambro, E. L., Gaston, C. J., Thornton, J. A., Laskin, A., Lin,
724 P., Wilson, J., Easter, R. C., Wang, J., Bertram, A. K., Martin, S. T., Seinfeld, J. H., and Worsnop, D. R.: Growth kinetics
725 and size distribution dynamics of viscous secondary organic aerosol, *Environ. Sci. Technol.*, 52, 1191-1199,
726 <https://doi.org/10.1021/acs.est.7b04623>, 2018.

727 Zeng, P., Sun, F., Liu, Y., Wang, Y., Li, G., and Che, Y.: Mapping future droughts under global warming across China: a
728 combined multi-timescale meteorological drought index and SOM-Kmeans approach, *Weather Clim. Extreme*, 31,
729 100304, <https://doi.org/10.1016/j.wace.2021.100304>, 2021.

730 Zhang, J., Lian, C., Wang, W., Ge, M., Guo, Y., Ran, H., Zhang, Y., Zheng, F., Fan, X., Yan, C., Daellenbach, K. R., Liu, Y.,
731 Kulmala, M., and An, J.: Amplified role of potential HONO sources in O₃ formation in North China Plain during
732 autumn haze aggravating processes, *Atmos. Chem. Phys.*, 22, 3275-3302, <https://doi.org/10.5194/acp-22-3275-2022>,
733 2022.

734 Zhang, Y., Chen, Y., Lei, Z., Olson, N. E., Riva, M., Koss, A. R., Zhang, Z., Gold, A., Jayne, J. T., Worsnop, D. R., Onasch, T.
735 B., Kroll, J. H., Turpin, B. J., Ault, A. P., and Surratt, J. D.: Joint impacts of acidity and viscosity on the formation of
736 secondary organic aerosol from isoprene epoxydiols (IEPOX) in phase separated particles, *ACS Earth Space Chem.*, 3,
737 2646-2658, <https://doi.org/10.1021/acsearthspacechem.9b00209>, 2019a.

738 Zhang, Y., Nichman, L., Spencer, P., Jung, J. I., Lee, A., Heffernan, B. K., Gold, A., Zhang, Z., Chen, Y., Canagaratna, M. R.,
739 Jayne, J. T., Worsnop, D. R., Onasch, T. B., Surratt, J. D., Chandler, D., Davidovits, P., and Kolb, C. E.: The cooling
740 rate- and volatility-dependent glass-forming properties of organic aerosols measured by broadband dielectric
741 spectroscopy, *Environ. Sci. Technol.*, 53, 12366-12378, <https://doi.org/10.1021/acs.est.9b03317>, 2019b.

742 Zheng, B., Tong, D., Li, M., Liu, F., Hong, C., Geng, G., Li, H., Li, X., Peng, L., Qi, J., Yan, L., Zhang, Y., Zhao, H., Zheng,
743 Y., He, K., and Zhang, Q.: Trends in China's anthropogenic emissions since 2010 as the consequence of clean air actions,
744 *Atmos. Chem. Phys.*, 18, 14095-14111, <https://doi.org/10.5194/acp-18-14095-2018>, 2018.

745 Ziemann, P. J. and Atkinson, R.: Kinetics, products, and mechanisms of secondary organic aerosol formation, *Chem. Soc.*
746 *Rev.*, 41, 6582-6605, <https://doi.org/10.1039/C2CS35122F>, 2012.

747

748 **Table 1.** Sensitivity calculations for evaluating the effects of simulated SOA volatility distributions (sensitivity case A), RH (sensitivity
749 case B) and the water absorbed by inorganic components (sensitivity case C) on viscosity estimations.

750

| Cases | C^* at 298 K and ΔH_{vap} in each volatility bin | The liquid water content considered in viscosity estimations | RH |
|--------------------|--|---|---|
| Base case | 0.1, 1, 10, 100, and 1000 $\mu\text{g m}^{-3}$ with ΔH_{vap} of 142, 131, 120, 109, and 98 kJ mol^{-1} | water absorbed by SOA particles with the assumption that SOA particles are externally mixed with inorganics | RH simulated by WRF-Chem |
| Sensitivity case A | 0.0001, 1, 10, 100, and 1000 $\mu\text{g m}^{-3}$ with ΔH_{vap} of 40, 131, 120, 109, and 98 kJ mol^{-1} | water absorbed by SOA particles with the assumption that SOA particles are externally mixed with inorganics | RH simulated by WRF-Chem |
| Sensitivity case B | 0.1, 1, 10, 100, and 1000 $\mu\text{g m}^{-3}$ with ΔH_{vap} of 142, 131, 120, 109, and 98 kJ mol^{-1} | water absorbed by SOA particles with the assumption that SOA particles are externally mixed with inorganics | RH simulated by WRF-Chem increased by a factor of 10% |
| Sensitivity case C | 0.1, 1, 10, 100, and 1000 $\mu\text{g m}^{-3}$ with ΔH_{vap} of 142, 131, 120, 109, and 98 kJ mol^{-1} | water absorbed by both SOA particles and inorganic components with the assumption that SOA particles are internally mixed with inorganics | RH simulated by WRF-Chem |

751

752

753

754

755

756

757

758

759

760

761

762

763

764

765

766

767

768

769

770

771

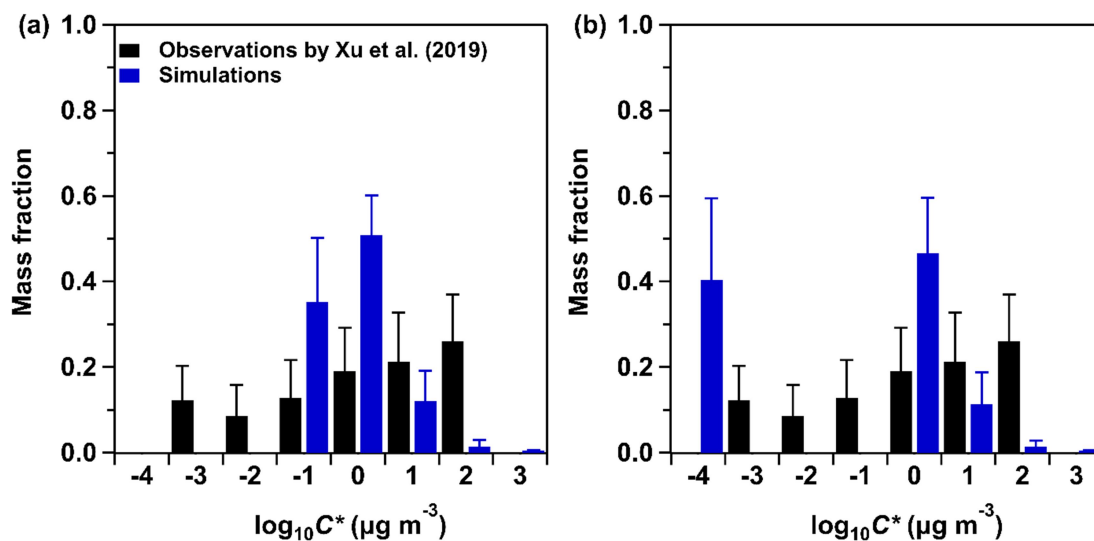
772

773

774

775

776



777

778 **Figure 1.** Comparison of the average volatility distributions of observed OOA and simulated SOA at the IAP site during 20 May – 23 June
 779 2018. The black bars represent the volatility distributions of observed OOA adopted from Xu et al. (2019). The blue bars represent the
 780 volatility distributions of SOA simulated by WRF-Chem, with five C^* bins set to be 0.1, 1, 10, 100, and 1000 $\mu\text{g m}^{-3}$ at 298 K in (a), and
 781 0.0001, 1, 10, 100, and 1000 $\mu\text{g m}^{-3}$ at 298 K in (b). The blue error bars represent the one standard deviation.

782

783

784

785

786

787

788

789

790

791

792

793

794

795

796

797

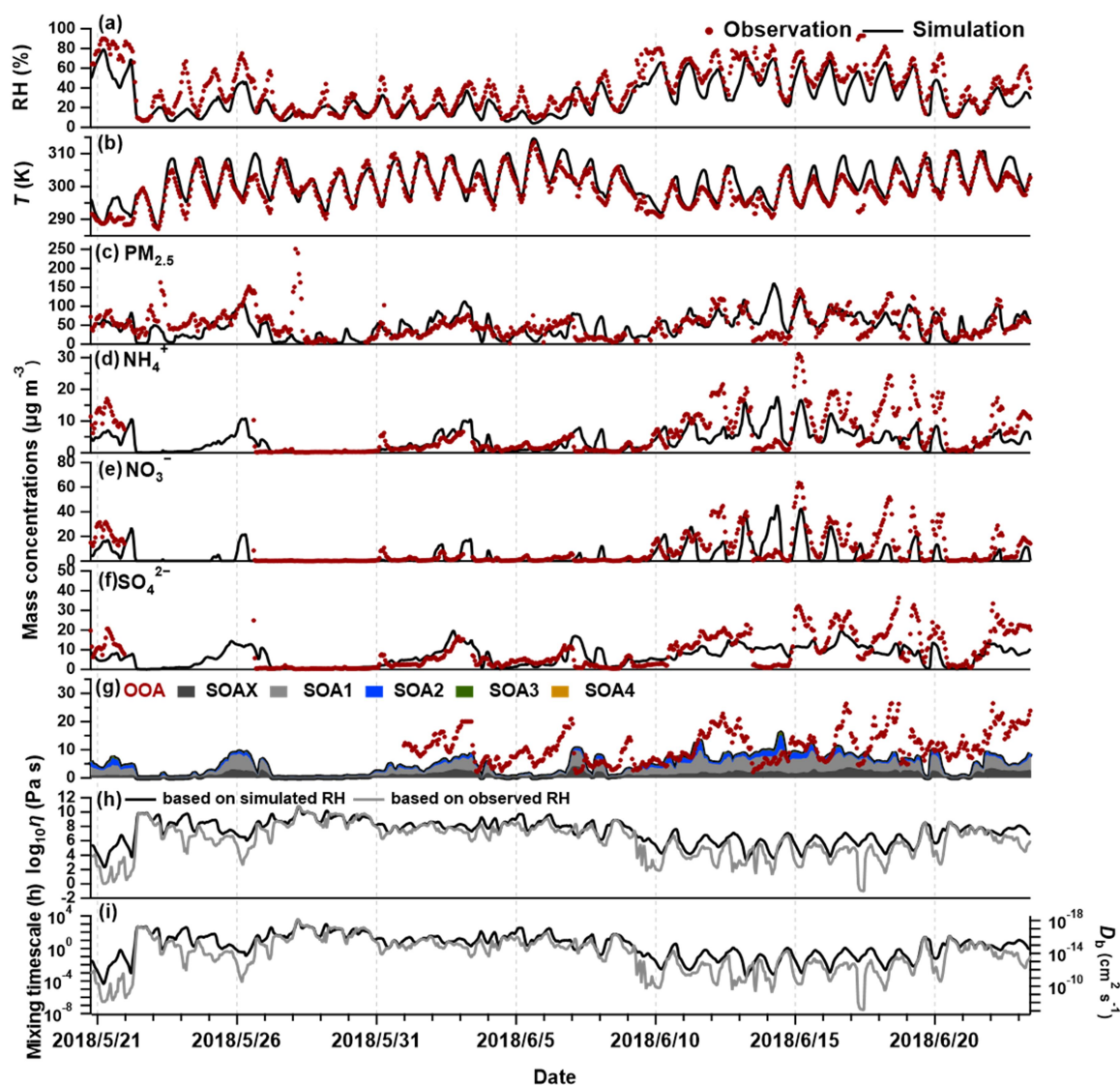
798

799

800

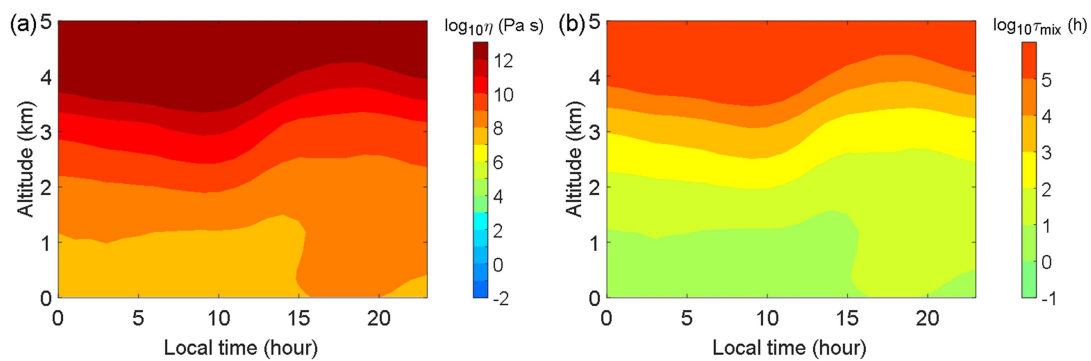
801

802



803
 804 **Figure 2.** Observations and simulations of temporal variations of (a) RH, (b) T , (c) $\text{PM}_{2.5}$ concentrations, (d) NH_4^+ concentrations, (e)
 805 NO_3^- concentrations, and (f) SO_4^{2-} concentrations at the IAP site. (g) Observed OOA concentrations (red dots) and simulated SOA
 806 concentrations, with SOAX, SOA1, SOA2, SOA3, and SOA4 represent the SOA with C^* of 0.1, 1, 10, 100, and 1000 $\mu\text{g m}^{-3}$ at 298 K,
 807 respectively. (h) SOA viscosity, and (i) bulk diffusion coefficients and mixing timescale of organic molecules within 200 nm SOA particles
 808 calculated using the RH simulated by the WRF-Chem model or the RH observed at the IAP site.

809
 810
 811
 812
 813
 814



815

816 **Figure 3.** Median diurnal and vertical profiles of estimated (a) SOA viscosity and (b) mixing timescales for organic molecules within 200
 817 nm SOA particles at the IAP site during May 20 – June 23 in 2018. Note: altitude is approximate and estimated from WRF pressure layers.

818

819

820

821

822

823

824

825

826

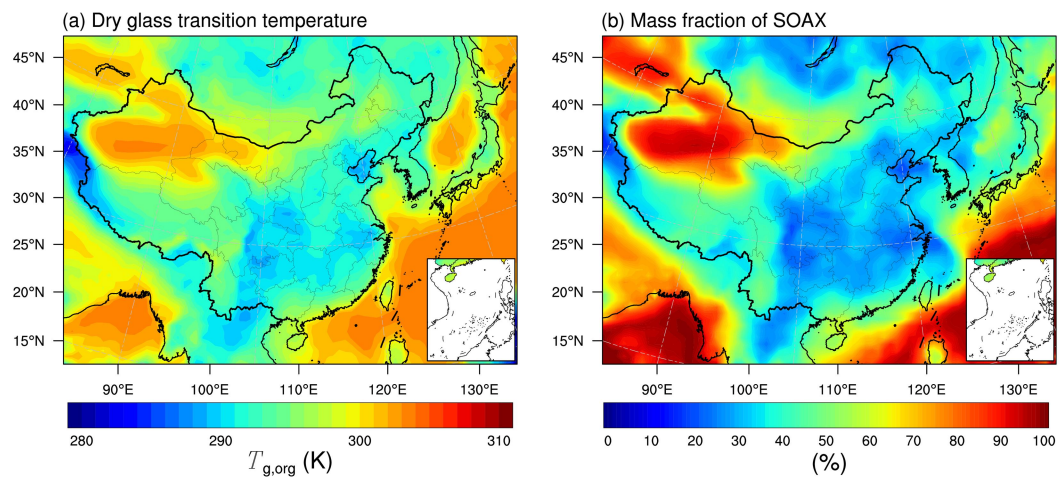
827

828

829

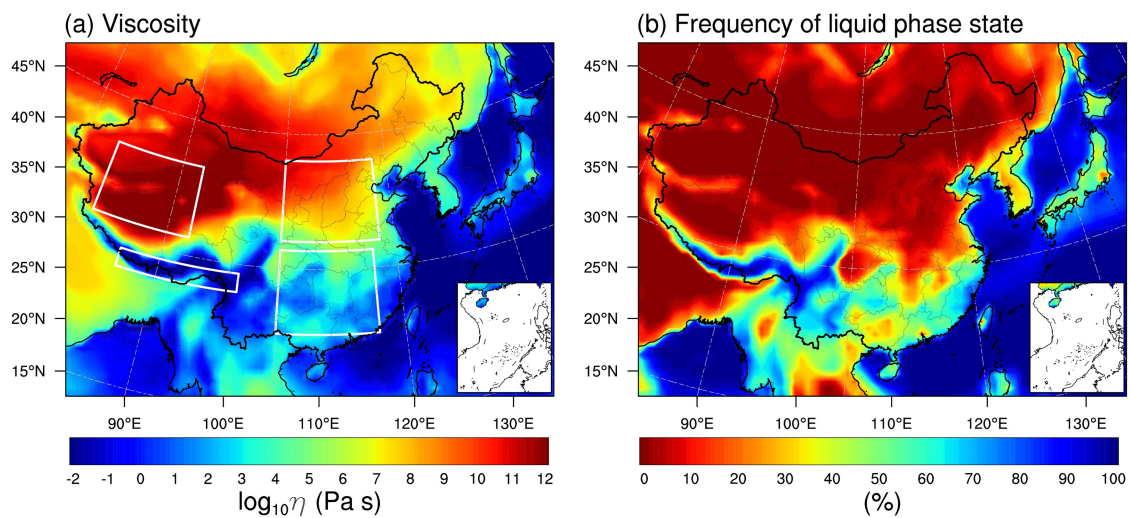
830

831



832
 833 **Figure 4.** The predicted median surface values of (a) glass transition temperature of SOA particles at the dry condition and (b) mass
 834 fractions of SOAX ($C^* = 0.1 \mu\text{g m}^{-3}$ at 298 K) during May 20 – June 23 in 2018 simulated in the base case (Table 1).

835
 836
 837
 838
 839
 840
 841
 842
 843
 844
 845
 846
 847
 848



849

850

Figure 5. WRF-Chem predicted (a) median surface values of viscosity and (b) the percent time that an organic aerosol particle is in the liquid phase state during May 20 – June 23 in 2018. The white boxes in panel (a) specify the selected regions in the northern China, southern China, northern Qinghai-Tibet Plateau, and southern Qinghai-Tibet Plateau.

851

852

853

854

855

856

857

858

859

860

861

862

863

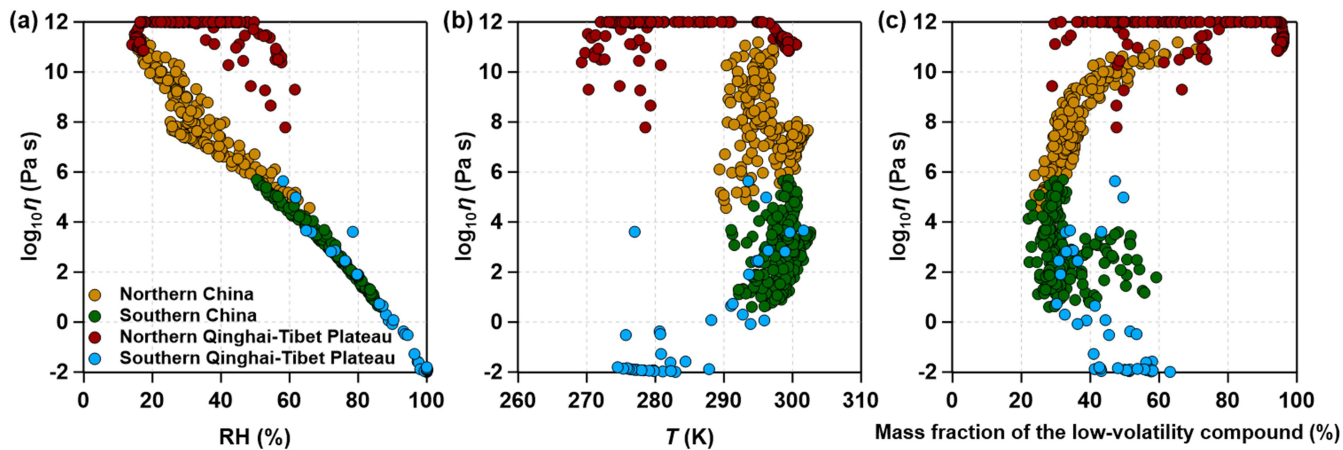
864

865

866

867

868



869

870 **Figure 6.** The median values of viscosity as a function of (a) RH, (b) T and (c) the mass fraction of SOAX ($C^* = 0.1 \mu\text{g m}^{-3}$ at 298 K)
 871 calculated for selected regions in the northern China, southern China, northern Qinghai-Tibet Plateau, and southern Qinghai-Tibet Plateau
 872 as specified by white boxes in Fig. 5a during May 20 – June 23 in 2018.

873

874

875

876

877

878

879

880

881

882

883

884

885

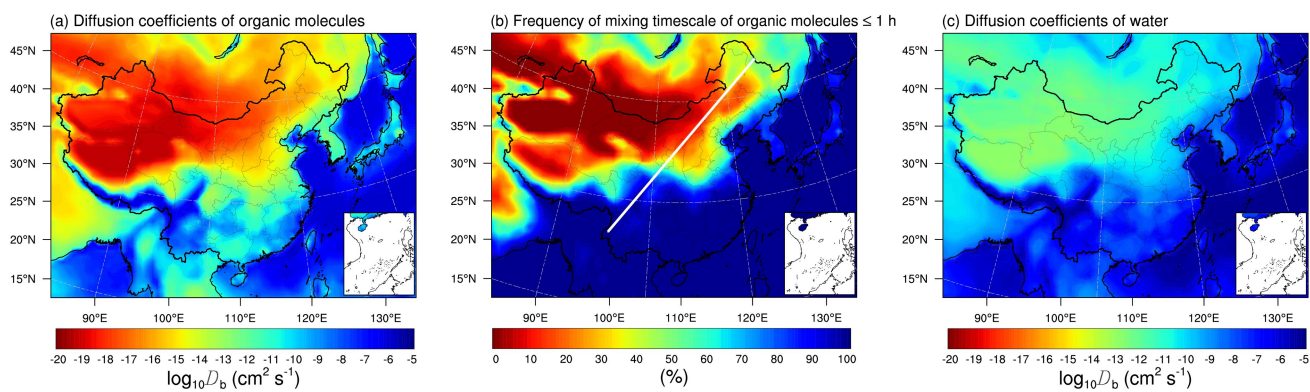
886

887

888

889

890



891

892 **Figure 7.** WRF-Chem predicted median surface values of the diffusion coefficients of (a) organic molecules and (c) water molecules in
 893 SOA particles. (b) The percent time that the mixing timescale of organic molecules in a 200 nm particle is less than 1 h during May 20 –
 894 June 23 in 2018. The white line indicates the “Hu Huanyong Line” (Hu, 1935).

895

896

897

898

899

900

901

902

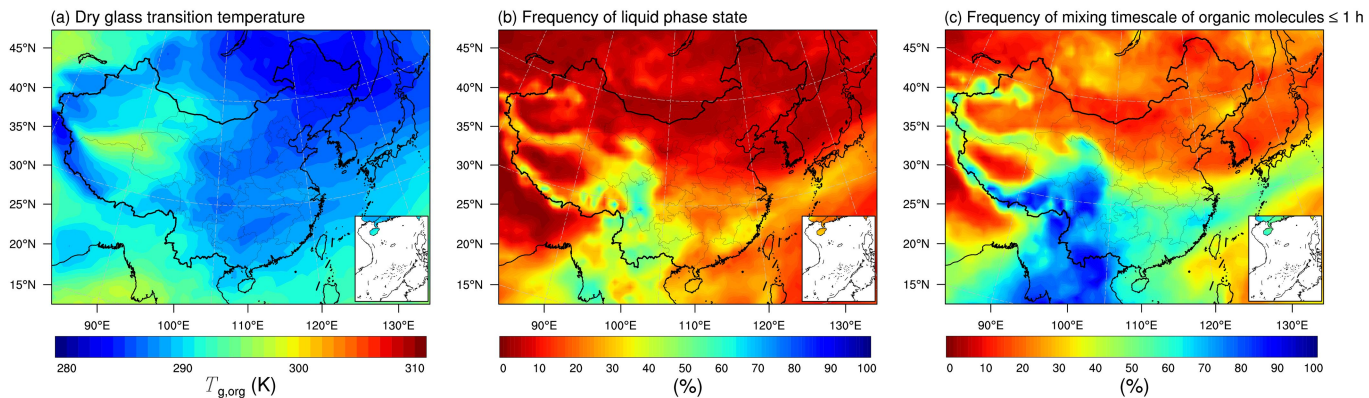
903

904

905

906

907



908

909 **Figure 8.** WRF-Chem predicted median values of (a) glass transition temperature of SOA particles at the dry condition, (b) the percent
 910 time that an organic aerosol particle is in the liquid phase state, and (c) the percent time that the mixing timescale of organic molecules in a
 911 200 nm particle is less than 1 h at 500 hPa during May 20 – June 23 in 2018.

912

913

914

915

916

917

918

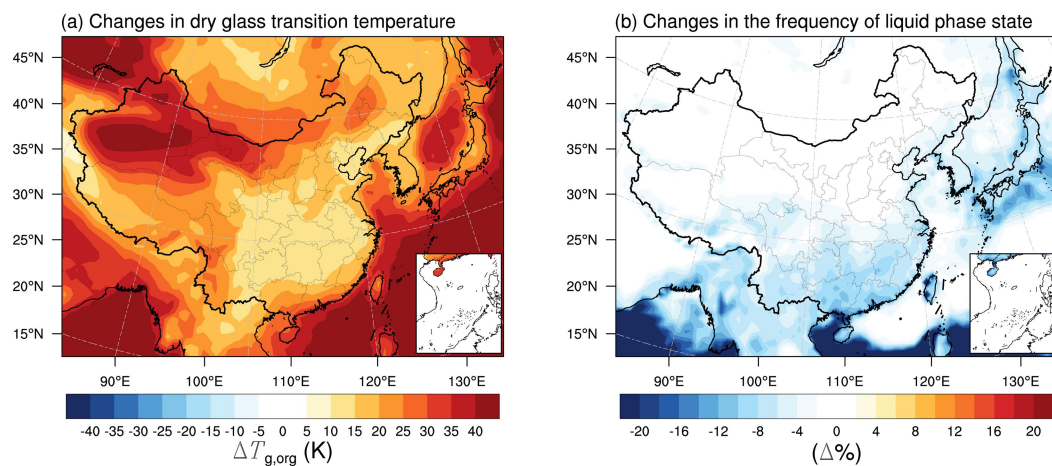
919

920

921

922

923



924

925 **Figure 9.** Modelled median differences of (a) glass transition temperature of SOA particles at the dry condition, and (b) the percent time
 926 that an organic aerosol particle is in the liquid phase state between a sensitivity case with the lowest C^* of $0.0001 \mu\text{g m}^{-3}$ at 298 K (ΔH_{vap} of
 927 40 kJ mol^{-1} , case A in Table 1) and a base case with the lowest C^* of $0.1 \mu\text{g m}^{-3}$ at 298 K (ΔH_{vap} of 142 kJ mol^{-1} , Table 1).

928

929

930

931

932

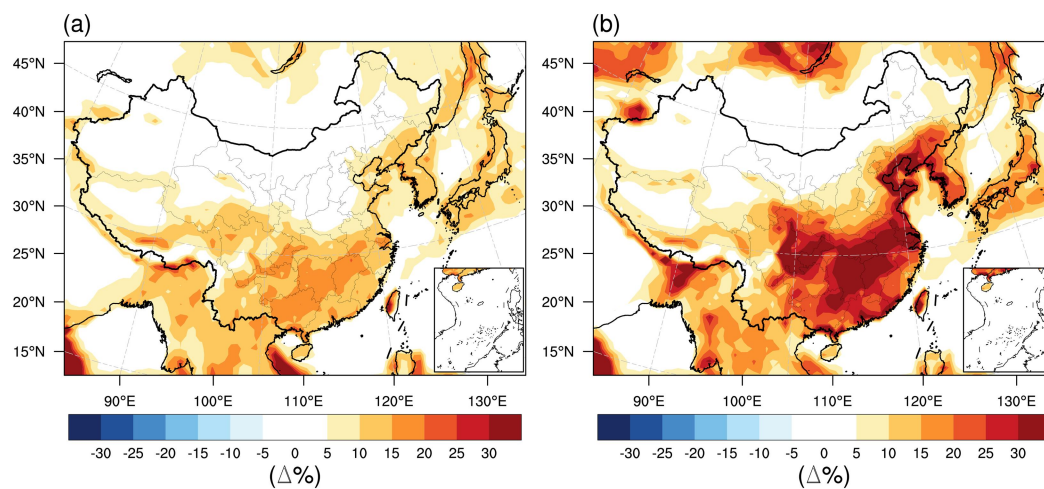
933

934

935

936

937



938
 939 **Figure 10.** (a) Impacts of RH on the percent time that an organic aerosol particle is in the liquid phase state: modelled median differences
 940 between a case with the WRF-Chem simulated RH increased by a factor of 10 % (case B, Table 1) and a base case (Table 1) with the
 941 WRF-Chem simulated RH. (b) Impacts of the water absorbed by inorganics on the percent time that an organic aerosol particle is in the
 942 liquid phase state: modelled median differences between a case considering the water absorbed by both SOA particles and inorganics (case
 943 C, Table 1) and a base case (Table 1) considering the water absorbed by SOA particles solely.

944
 945